Topological superconductivity induced by spin-orbit coupling, perpendicular magnetic field, and superlattice potential

Jonathan Schirmer, J. K. Jain ⓘ, and C. -X. Liu

Department of Physics, 104 Davey Lab, The Pennsylvania State University, University Park, Pennsylvania 16802, USA

Topological superconductors support Majorana modes, which are quasiparticles that are their own antiparticles and obey non-Abelian statistics in which successive exchanges of particles do not always commute. Here we investigate whether a two-dimensional superconductor with ordinary *s*-wave pairing can be rendered topological by the application of a strong magnetic field. To address this, we obtain the self-consistent solutions to the mean-field Bogoliubov–de Gennes equations, which are a large set of nonlinearly coupled equations, for electrons moving on a lattice. We find that the topological "quantum Hall superconductivity" is facilitated by a combination of spin-orbit coupling, which locks an electron's spin to its momentum as it moves through a material, and a coupling to an external periodic potential which gives a dispersion to the Landau levels and also distorts the Abrikosov lattice. We find that, for a range of parameters, the Landau levels broadened by the external periodic potential support topological superconductivity, which is typically accompanied by a lattice of "giant" h/e vortices as opposed to the familiar lattice of $h/2e$ Abrikosov vortices. In the presence of a periodic potential, we find it necessary to use an ansatz for the pairing potential of the form $\Delta(\boldsymbol{r})e^{i2\boldsymbol{Q}\cdot\boldsymbol{r}}$ where $\Delta(\boldsymbol{r})$ has a periodicity commensurate with the periodic potential. However, despite this form of the pairing potential, the current in the ground state is zero. In the region of ordinary superconductivity, we typically find a lattice of dimers of $h/2e$ vortices. Our work suggests a realistic proposal for achieving topological superconductivity, as well as a helical order parameter and unusual Abrikosov lattices.

I. INTRODUCTION

Majorana modes, which are quasiparticles that are their own antiparticles, are perhaps the most readily realizable non-Abelian anyons. In topological superconductors, they appear as zero-energy quasiparticles which reside in the cores of Abrikosov vortices, or appear as chiral boundary modes. Their non-Abelian braid statistics, although not yielding all unitary gates, are a step toward the goal of topological quantum computation with anyons [1–14]. Besides their potential application for quantum computation and being of fundamental scientific interest, achieving Majorana modes in the laboratory could lead to a physical realization of interesting theoretical models, such as the Sachdev-Ye-Kitaev model [15]. There are several candidate condensed matter systems which are thought to host Majorana modes, including the $\nu = 5/2$ fractional quantum Hall effect, two-dimensional *p*-wave superconductors, and two-dimensional films of ^{3}He-A superfluid [16]. In addition, there have been proposals to engineer topologically interesting structures which host Majorana modes. In particular, topological *p*-wave superconductivity (SC) is thought to arise when a spin-orbit-coupled electron gas is proximity coupled to an *s*-wave superconductor, owing to the appearance of a single Fermi surface in certain parameter regimes [4,17–29]. Particularly notable are proposals for quasi-one-dimensional systems, e.g., semiconductor wires [19,21,25,30–33], magnetic atom chains [34–38], and planar Josephson junctions [39,40], for realizing topological superconductivity (TSC). Some exciting progress has been made on these fronts [41].

In earlier work, Sau *et al.* proposed a heterostructure consisting of a spin-orbit-coupled two-dimensional electron gas (2DEG) coupled to a ferromagnetic insulator and an *s*-wave superconductor [4,21]. The ferromagnetic insulator causes a gap in the single-particle spectrum of the 2DEG at zero momentum. This gap, along with spin-orbit coupling (SOC), leads to the appearance of a single Fermi surface for certain values of the chemical potential. When the system is coupled to an *s*-wave superconductor, effective chiral *p*-wave TSC is realized in a single band. They studied the properties of the Bogoliubov–de Gennes (BdG) spectrum in the regime where vortices are well separated. Crucially for these works, it is the SOC, together with the Zeeman-like effect from the magnetic insulator, which gives rise to the topological phase.

A related idea is to apply a magnetic field to a two-dimensional system, utilizing the orbital effect to realize TSC. Indeed the topological nature of the underlying Landau levels (LLs) sets the stage nicely for TSC when a pairing gap is opened [20,23]. The combination of SC and quantum Hall (QH) systems, both integer (IQHE) and fractional (FQHE), has been thought to be fertile ground for the realization not only of TSC with the concomitant Majorana particles, but also more exotic topological phases that are predicted to harbor parafermions and Fibonacci anyons [42–50]. In order to integrate the orbital effect of the magnetic field and SC, there are, broadly speaking, two approaches. The first, like the above proposal, involves proximity coupling a QH system to a superconductor. It is necessary to take into account the vortices in superconductors exposed to a magnetic field [51–55]. Zocher and Rosenow [51], Mishmash *et al.* [52],

and Chaudhary and MacDonald [54] showed that there is no TSC for particles in the lowest LL (or the lowest few LLs) if the unit cell of the Abrikosov lattice has only one (or in general an odd number of) superconducting flux quanta (that is, the unit cell violates magnetic translation symmetry), as is the case for the usual triangular Abrikosov lattice or even a square Abrikosov lattice. It was shown that the spectrum of the BdG equations, which is completely determined by the s-wave pairing potential when the normal state bands are flat, has an even degeneracy in the case of a square or triangular Abrikosov vortex lattice, and therefore any quasiparticle spectral gap closing across a topological phase transition must lead to a Chern number change by an even integer, thereby precluding the appearance of TSC that requires odd-integer Chern number. All of these works considered LLs with SOC. Also, because they considered proximity-induced SC, they did not need to find a self-consistent mean-field state within the 2DEG, since the pairing and, consequently, the Abrikosov lattice are inherited from a nearby bulk superconductor, and hence are a part of the Hamiltonian defining the problem, not of its solution.

The second approach is to apply a strong magnetic field to an intrinsic two-dimensional superconductor, driving it into the Landau level limit. It has been known for some time that BCS mean-field theory predicts that superconductivity can be enhanced due to the Landau level structure of systems in a strong magnetic field [56–74]. Because of the enlargement of the density of states in Landau levels, it has been predicted that the critical temperature in this limit approaches that of the zero-field value [57,58]. This has been referred to as quantum Hall superconductivity [74]. In contrast to the case of proximity-coupled SC in LLs, the vortex lattice structure is determined by electrons pairing in LLs within the same sample, and consequently a vortex lattice structure cannot be assumed but must be solved for self-consistently [60,64,68]. In spite of extensive theoretical efforts, convincing experimental demonstrations of these remarkable predictions have been lacking. In addition, to our knowledge, there has not been any study of the possibility of topological superconductivity in such systems. That is the focus of the present study.

In this work, we explore if TSC can arise from pairing between electrons occupying LLs, which may be referred to as "quantum Hall topological superconductivity." For this purpose, we consider a fully self-consistent mean-field theory of a lattice model under a magnetic field with a phenomenological attractive on-site Hubbard interaction. We also consider Rashba SOC and a periodic superlattice potential. We numerically determine phase diagrams without SOC or superlattice potential, with SOC and without superlattice potential, without SOC and with superlattice potential, and with both SOC and superlattice potential. We find that while SOC is necessary for TSC, the application of a superlattice potential markedly enlarges the regions hosting TSC in the phase diagram. The reason is because the Abrikosov lattice distorted by the superlattice potential has more than one superconducting flux quantum in a unit cell. (As shown below, the TSC often occurs in regions where two Abrikosov vortices merge into a "giant" vortex.) A schematic phase diagram is shown in Fig. 1.
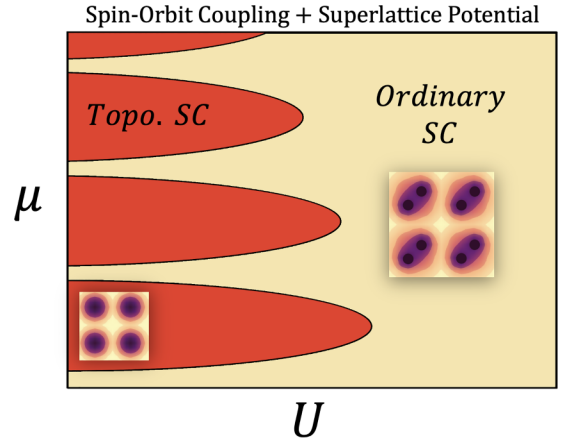

FIG. 1. A schematic of the numerically determined phase diagram in the presence of both spin-orbit coupling and a superlattice potential as a function of the strength of the on-site attractive interaction $-U$ and the chemical potential μ. The regions of topological superconductivity (TSC), depicted in red, roughly coincide with Landau levels broadened by the superlattice potential. The vortices here typically tend to form a lattice of "giant" vortices (as shown in the bottom left of the figure), where a giant vortex consists of two superconducting vortices merged into one. In the regions of ordinary superconductivity (shaded yellow), the vortices typically form a lattice of dimers as depicted on the right of the figure. The vortex lattices are square because of our choice of a square superlattice potential.

More detailed phase diagrams are given below. In order to properly treat systems with a superlattice potential, we find it necessary to consider helical pairing functions, which describe Cooper pairs with nonzero center-of-mass momentum. This ansatz is the same as the one employed by Fulde and Ferrell [75]. We also describe vortex lattice structures arising in our model, some of which are quite unexpected. We finally discuss some prospective experimental realizations of this model.

II. MODEL

A. Hamiltonian

We consider spin-$\frac{1}{2}$ fermions on a square lattice in a magnetic field with Rashba SOC, a single-particle potential, and on-site attractive interaction. The interacting Hamiltonian is

$$\mathcal{H} = \mathcal{H}_0 + \mathcal{H}_{\text{SO}} + \mathcal{H}_{\text{I}}, \tag{1}$$

where

$$\mathcal{H}_0 = -\sum_{j,\delta,\sigma}(e^{iA_\delta(\mathbf{r}_j)}c^\dagger_{j+\delta,\sigma}c_{j,\sigma} + e^{-iA_\delta(\mathbf{r}_j)}c^\dagger_{j,\sigma}c_{j+\delta,\sigma})$$
$$- \sum_{j,\sigma}(\mu - V(\mathbf{r}_j))c^\dagger_{j,\sigma}c_{j,\sigma},$$

$$\mathcal{H}_{\text{SO}} = V_{\text{SO}}\sum_j(e^{iA_{\hat{x}x}(\mathbf{r}_j)}(c^\dagger_{j+\hat{x}x,\downarrow}c_{j,\uparrow} - c^\dagger_{j+\hat{x}x,\uparrow}c_{j,\downarrow})$$
$$+ ie^{iA_{\hat{y}y}(\mathbf{r}_j)}(c^\dagger_{j+\hat{y}y,\downarrow}c_{j,\uparrow} + c^\dagger_{j+\hat{y}y,\uparrow}c_{j,\downarrow})) + \text{H.c.},$$

$$\mathcal{H}_{\text{I}} = -U\sum_j c^\dagger_{j,\uparrow}c^\dagger_{j,\downarrow}c_{j,\downarrow}c_{j,\uparrow}, \tag{2}$$

where $\boldsymbol{r}_j$ is the location of site j, V_{SO} is the SOC strength, μ is the chemical potential, U is the interaction strength, $A_\delta(\boldsymbol{r}_j)$ are the hopping (Peierls) phases, $\delta = \hat{\boldsymbol{x}}, \hat{\boldsymbol{y}}$, and $\sigma = \uparrow, \downarrow$. The annihilation (creation) operators for fermions of spin σ at site j are $c_{j,\sigma}$ ($c_{j,\sigma}^\dagger$). We have set the hopping amplitude to unity. Note that $A_\delta(\boldsymbol{r}_j)$ appears both in the hopping term and in the SOC term, which is necessary for gauge invariance. The Rashba SOC takes the form of the lattice-discretized version of $H_R = \alpha \hat{z} \cdot (\boldsymbol{\sigma} \times \boldsymbol{\pi})$ where $\boldsymbol{\pi}$ is the kinematic momentum (further discussion of this term can be found in the Supplemental Material (SM) [76]). Finally, we include a periodic single-particle potential of the form

$$V(\boldsymbol{r}) = -\frac{V_{\text{sp}}}{2} \sum_{\delta = \hat{x}x, \hat{y}y} \cos(\boldsymbol{\eta}_\delta \cdot \boldsymbol{r}), \tag{3}$$

where V_{sp} is the strength of the periodic superlattice potential and η_x and η_y are the wave vectors of the periodic superlattice potential in the x and y directions, respectively.

B. Magnetic unit cell

A discussion of the translation symmetries of the noninteracting part of the Hamiltonian, i.e., $\mathcal{H}_0 + \mathcal{H}_{\text{SO}}$, is in order—we will discuss the interacting part $\mathcal{H}_I$ below. The magnetic field in our model is chosen so that the magnetic flux through each square plaquette of the lattice is the same rational fraction $\alpha = 1/q$ of the flux quantum $\Phi_0 = h/e$. This rational fraction, and in particular the denominator q, determines the translation properties of the noninteracting Hamiltonian by constraining the unit cell of the system—called the magnetic unit cell (MUC)—to have a multiple of q sites [77–82]. For our calculation, we choose $q = 64$ and take the MUC to be a square consisting of 16×16 sites. The total flux through this magnetic unit cell is four flux quanta. We will take the pairing potential to have the same periodicity as the MUC. This choice of MUC allows for triangular, square, and dimerized lattice structures for the Abrikosov flux lattice. (We note that the smallest choice would be an 8×8 MUC, which encloses one flux quantum, but that does not allow a triangular lattice of Abrikosov vortices. We have also examined several cases for other MUC types at the same magnetic field, such as 4×64 with four flux quanta per MUC, and found that in all these cases the energies were higher than those obtained with the 16×16 MUC.)

The single-particle potential $V(\boldsymbol{r})$ is chosen to be commensurate with the MUC, and in particular we take $(\eta_x, \eta_y) = (\frac{2\pi}{8}, \frac{2\pi}{8})$. Previous authors [51,52,54] have emphasized the need to break the translation symmetry of the vortex lattice in order to realize TSC in the presence of Abrikosov vortices. Our choice of single-particle potential accomplishes this, since the unit cell for the periodic potential contains one flux quantum h/e. In experiments, we expect that the magnetic length can be tuned to the wavelength of the periodic single-particle superlattice potential by tuning the magnetic field.

C. Mean-field theory

A mean-field factorization of the interacting part of the Hamiltonian $\mathcal{H}_I$ is performed in the pairing channel

$$\mathcal{H}_I = -U \sum_j c_{j,\uparrow}^\dagger c_{j,\downarrow}^\dagger c_{j,\downarrow} c_{j,\uparrow}$$

$$\rightarrow -U \sum_j (\langle c_{j,\downarrow} c_{j,\uparrow} \rangle c_{j,\uparrow}^\dagger c_{j,\downarrow}^\dagger + \langle c_{j,\uparrow}^\dagger c_{j,\downarrow}^\dagger \rangle c_{j,\downarrow} c_{j,\uparrow}$$

$$- \langle c_{j,\uparrow}^\dagger c_{j,\downarrow}^\dagger \rangle \langle c_{j,\downarrow} c_{j,\uparrow} \rangle). \tag{4}$$

In this work, we consider a mean-field ansatz of the form

$$\mathcal{H}_I \rightarrow \mathcal{H}_\Delta = -\sum_j \Delta_j e^{i2\boldsymbol{Q} \cdot \boldsymbol{r}_j} c_{j,\uparrow}^\dagger c_{j,\downarrow}^\dagger + \text{H.c.} + \sum_j \frac{|\Delta_j|^2}{U}, \tag{5}$$

where the field Δ_j is assumed to be periodic with the same periodicity as the MUC. The vector $\boldsymbol{Q}$, which we will refer to as a boost vector, is treated as a variational parameter; the optimum $\boldsymbol{Q}$ is that which leads to a mean-field ground state with the lowest energy. Note that, due to the phase factor $e^{i2\boldsymbol{Q} \cdot \boldsymbol{r}_j}$, the pairing potential in this model is *not* necessarily periodic. The addition of this phase factor gives the superconducting condensate a finite momentum $2\boldsymbol{Q}$ [83–87], although the ground state with nonzero $\boldsymbol{Q}$ does not carry a finite net current. This admits a short proof: since we are to minimize the energy with respect to $\boldsymbol{Q}$, we must have $\frac{\delta \mathcal{E}_{\text{MF}}}{\delta \boldsymbol{Q}} = 0$, where $\mathcal{E}_{\text{MF}}$ is the energy. However $\frac{\delta \mathcal{E}_{\text{MF}}}{\delta \boldsymbol{Q}}$ is also the net current (see Appendix A). Thus, it vanishes in the ground state.

The self-consistency equations are

$$\Delta_j e^{i2\boldsymbol{Q} \cdot \boldsymbol{r}_j} = U \langle \Gamma | c_{j,\downarrow} c_{j,\uparrow} | \Gamma \rangle, \tag{6}$$

where $|\Gamma\rangle$ is the mean-field ground state. In order to solve this equation, we first make a boost transformation on the mean-field Hamiltonian. A similar transformation has been employed in studies of helical phases in noncentrosymmetric superconductors [84–86]. We define boost operators $U_B(\boldsymbol{Q})$ which act on the creation operators in position space as

$$\bar{c}_{i,\sigma} \equiv U_B^\dagger(\boldsymbol{Q}) c_{i,\sigma} U_B(\boldsymbol{Q}) = c_{i,\sigma} e^{i\boldsymbol{Q} \cdot \boldsymbol{r}_i}, \tag{7}$$

where the bar over the operators is meant to denote operators in a boosted "frame." The mean-field Hamiltonian, defined as $\mathcal{H}_{\text{MF}} = \mathcal{H}_0 + \mathcal{H}_{\text{SO}} + \mathcal{H}_\Delta$, is transformed using the boost operators. The action of the boosts on the terms $\mathcal{H}_0$ and $\mathcal{H}_{\text{SO}}$ has the effect of shifting the hopping phases by $A(\boldsymbol{r}_j) \rightarrow A(\boldsymbol{r}_j) - \boldsymbol{Q}$. The boost has the effect on $\mathcal{H}_\Delta$ of canceling the phase factor $e^{i2\boldsymbol{Q} \cdot \boldsymbol{r}_j}$. In other words,

$$\bar{\mathcal{H}}_\Delta = U_B^\dagger(\boldsymbol{Q}) \mathcal{H}_\Delta U_B(\boldsymbol{Q})$$

$$= -\sum_j \Delta_j c_{j,\uparrow}^\dagger c_{j,\downarrow}^\dagger + \text{H.c.} + \sum_j \frac{|\Delta_j|^2}{U}. \tag{8}$$

Thus, the pairing Hamiltonian in the barred frame has the same periodicity as $\bar{\mathcal{H}}_0$ and $\bar{\mathcal{H}}_{\text{SO}}$, and we can make use of the BdG formalism, using the magnetic Bloch basis, to solve the mean-field problem. The self-consistency equations in the barred frame are

$$\Delta_j = U \langle \bar{\Gamma} | c_{j,\downarrow} c_{j,\uparrow} | \bar{\Gamma} \rangle, \tag{9}$$

where $|\bar{\Gamma}\rangle = U_B^\dagger(\boldsymbol{Q})|\Gamma\rangle$ is the mean-field ground state in the barred frame.

D. Bogoliubov–de Gennes formalism

The mean-field Hamiltonian in the boosted frame can be expressed in terms of a BdG Hamiltonian by first transforming it into (magnetic) momentum space using the formula $c_{j,\sigma} = \frac{1}{L} \sum_{\boldsymbol{k}} e^{i\boldsymbol{k}\cdot\boldsymbol{R}_j} c_{\tilde{j},\sigma}(\boldsymbol{k})$, where $\boldsymbol{R}_j$ is the coordinate of the origin of the MUC in which site j resides and $\tilde{j}$ denotes the site *within* the MUC of site j. In other words, $\boldsymbol{r}_j = \boldsymbol{R}_j + \tilde{\boldsymbol{r}}_j$, where $\tilde{\boldsymbol{r}}_j$ is the coordinate of $\tilde{j}$ (relative to the origin of the MUC). L is the number of MUCs in both the x and y directions; we consider L large enough so that the results are converged to the thermodynamic limit, where we define convergence according to the following criterion: a solution Δ_j^L to Eq. (9) with system size L is said to be converged to the thermodynamic limit if it is also a solution to Eq. (9) with system size $L+2$ to within the tolerance of the iterative algorithm used to solve Eq. (9) (see Appendix C for more details on the algorithm). Generally, we find that we need $L \geqslant 32$ for a 16×16 MUC for the pairing potential to be well converged. We also note that the Chern number (discussed below) is well converged for much smaller system size: $L \approx 6$ for a 16×16 MUC using a 24×24 momentum space grid for the Chern number calculation (see Sec. II G below).

The mean-field Hamiltonian may be written as

$$\mathcal{H}_{\mathrm{MF}} = \frac{1}{2} \sum_{\boldsymbol{k}} \sum_{\alpha,\beta=1}^{4N_{\mathrm{site}}} \psi_\alpha^\dagger(\boldsymbol{k})(H_{\mathrm{BdG}}(\boldsymbol{k}))_{\alpha\beta}\psi_\beta(\boldsymbol{k})$$
$$+ \frac{1}{2} \sum_{\boldsymbol{k}} \mathrm{Tr}[h(\boldsymbol{k})] + \sum_j \frac{|\Delta_j|^2}{U}, \qquad (10)$$

where the $\psi_\alpha(\vec{k})$ are defined by

$$\begin{pmatrix} \psi_{\tilde{j}}(\boldsymbol{k}) \\ \psi_{\tilde{j}+N_{\mathrm{site}}}(\boldsymbol{k}) \\ \psi_{\tilde{j}+2N_{\mathrm{site}}}(\boldsymbol{k}) \\ \psi_{\tilde{j}+3N_{\mathrm{site}}}(\boldsymbol{k}) \end{pmatrix} = \begin{pmatrix} c_{\tilde{j},\uparrow}(\boldsymbol{k}) \\ c_{\tilde{j},\downarrow}(\boldsymbol{k}) \\ c_{\tilde{j},\uparrow}^\dagger(-\boldsymbol{k}) \\ c_{\tilde{j},\downarrow}^\dagger(-\boldsymbol{k}) \end{pmatrix} \qquad (11)$$

for $\tilde{j} = 1, \ldots, N_{\mathrm{site}}$ and

$$H_{\mathrm{BdG}}(\boldsymbol{k})$$
$$= \begin{pmatrix} h(\boldsymbol{k}) & \Sigma(\boldsymbol{k}) & 0 & \Delta_{\uparrow\downarrow}(\boldsymbol{k}) \\ \Sigma^\dagger(\boldsymbol{k}) & h(\boldsymbol{k}) & \Delta_{\downarrow\uparrow}(\boldsymbol{k}) & 0 \\ 0 & -\Delta_{\uparrow\downarrow}^*(-\boldsymbol{k}) & -h^*(-\boldsymbol{k}) & -\Sigma^*(-\boldsymbol{k}) \\ -\Delta_{\downarrow\uparrow}^*(-\boldsymbol{k}) & 0 & -\Sigma^T(-\boldsymbol{k}) & -h^*(-\boldsymbol{k}) \end{pmatrix}$$
$$(12)$$

is the BdG Hamiltonian. N_{site} is the number of sites in the MUC. Each entry in Eq. (12) represents a matrix: $h(\boldsymbol{k})$ contains all the elements for hoppings (in the barred frame), the chemical potential, and the single-particle potential; $\Sigma(\boldsymbol{k})$ contains the SOC elements (in the barred frame); and $\Delta_{\uparrow\downarrow}(\boldsymbol{k})$ contains the pairing elements. Fermi statistics and Hermiticity imply $\Delta_{\downarrow\uparrow}^T(\boldsymbol{k}) = -\Delta_{\uparrow\downarrow}(-\boldsymbol{k})$. In

our model, $\Delta_{\uparrow\uparrow}(\boldsymbol{k}) = \Delta_{\downarrow\downarrow}(\boldsymbol{k}) = 0$ and $\Delta_{\downarrow\uparrow}(\boldsymbol{k}) = -\Delta_{\uparrow\downarrow}(\boldsymbol{k}) = \mathrm{diag}(\Delta_{\tilde{j}})$. Note that $H_{\mathrm{BdG}}(\boldsymbol{k})$ is particle-hole symmetric: $\mathcal{P}^{-1}H_{\mathrm{BdG}}(\boldsymbol{k})\mathcal{P} = -H_{\mathrm{BdG}}(-\boldsymbol{k})$ with $\mathcal{P} = \mathcal{K}\tau_x$, where τ_x is a Pauli matrix acting on the particle and hole subspaces and $\mathcal{K}$ is complex conjugation. This symmetry and its implications are further discussed in the SM [76].

We define the BdG quasiparticle creation operators as

$$\gamma_\beta^\dagger(\boldsymbol{k}) = \sum_{\alpha=1}^{4N_{\mathrm{site}}} \psi_\alpha^\dagger(\boldsymbol{k})\mathcal{U}_{\alpha\beta}(\boldsymbol{k}). \qquad (13)$$

By assumption, these are eigenoperators, so

$$[\mathcal{H}_{\mathrm{MF}}, \gamma_\beta^\dagger(\boldsymbol{k})] = E_\beta(\boldsymbol{k})\gamma_\beta^\dagger(\boldsymbol{k}), \qquad (14)$$

which implies that the columns of $\mathcal{U}_{\alpha\beta}$ must be eigenvectors of the BdG Hamiltonian,

$$\sum_{\alpha=1}^{4N_{\mathrm{site}}} (H_{\mathrm{BdG}}(\boldsymbol{k}))_{\delta\alpha}\mathcal{U}_{\alpha\beta}(\boldsymbol{k}) = E_\beta(\boldsymbol{k})\mathcal{U}_{\delta\beta}(\boldsymbol{k}). \qquad (15)$$

We identify Eqs. (15) as the BdG equations. The ground state $|\bar{\Gamma}\rangle$ is obtained by filling the vacuum with the negative-energy BdG quasiparticle states. The mean-field ground-state energy is given by

$$\mathcal{E}_{\mathrm{MF}} = \frac{1}{2} \sum_{E_\beta(\boldsymbol{k})<0} E_\beta(\boldsymbol{k}) + \frac{1}{2} \sum_{\boldsymbol{k}} \mathrm{Tr}[h(\boldsymbol{k})] + \sum_j \frac{|\Delta_j|^2}{U}. \quad (16)$$

E. Self-consistency equations

To solve the self-consistency equations, we define the Gor'kov Green's function at momentum $\boldsymbol{k}$ as

$$\mathcal{G}_{\alpha\beta}(\boldsymbol{k}) = \langle \psi_\alpha^\dagger(\boldsymbol{k})\psi_\beta(\boldsymbol{k})\rangle$$
$$= \sum_{m,n=1}^{4N_{\mathrm{site}}} \mathcal{U}_{m\alpha}^\dagger(\boldsymbol{k})\langle\gamma_m^\dagger(\boldsymbol{k})\gamma_n(\boldsymbol{k})\rangle\mathcal{U}_{\beta n}(\boldsymbol{k})$$
$$= \sum_{m=1}^{4N_{\mathrm{site}}} \mathcal{U}_{m\alpha}^\dagger(\boldsymbol{k})\mathcal{U}_{\beta m}(\boldsymbol{k})f(E_m(\boldsymbol{k})), \qquad (17)$$

where $f(E) = \frac{1}{\exp(E/k_BT)+1}$ is the Fermi-Dirac distribution function. We consider only $T=0$ in this work. The self-consistency equations can be expressed in terms of $\mathcal{G}$ as

$$\Delta_j = U\langle\bar{\Gamma}|c_{j,\downarrow}c_{j,\uparrow}|\bar{\Gamma}\rangle$$
$$= \frac{U}{L^2} \sum_{\boldsymbol{k},\boldsymbol{k}'} e^{i(\boldsymbol{k}+\boldsymbol{k}')\cdot\boldsymbol{R}_j}\langle\bar{\Gamma}|c_{\tilde{j},\downarrow}(\boldsymbol{k}')c_{\tilde{j},\uparrow}(\boldsymbol{k})|\bar{\Gamma}\rangle$$
$$= \frac{U}{L^2} \sum_{\boldsymbol{k}} \mathcal{G}_{\tilde{j}+3N_{\mathrm{site}},\tilde{j}}(\boldsymbol{k}). \qquad (18)$$

This equation is solved iteratively to achieve self-consistency.

F. Rationale for boosts

We consider superconductivity arising from Landau levels which are broadened by the presence of the single-particle potential in Eq. (3). A portion of the normal-state spectrum (i.e., the energies of $\mathcal{H}_0 + \mathcal{H}_{\mathrm{SO}}$) is shown in Fig. 2. Each band is spin split due to the presence of SOC and, in contrast
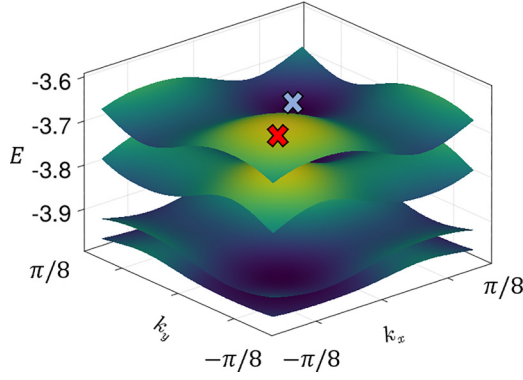
FIG. 2. The energies of broadened Landau levels plotted in the magnetic Brillouin zone. The single-particle potential strength is $V_{sp} = 0.2$ (in units where the hopping amplitude is set to unity). The flux per plaquette is $\alpha = 1/64$. The Rashba SOC strength is $V_{SO} = 0.1$. Because of the presence of the single-particle potential, the Landau levels become dispersive, and because of the SOC, the spin degeneracy is lifted. The maximum and minimum of the top band, which like the maxima and minima of other bands occur at finite momentum, are marked with a red and blue X, respectively.

to a system without a single-particle potential, the Landau levels are broadened and acquire a dispersion. The minima and maxima of the bands occur at nonzero momenta and consequently a pairing Hamiltonian describing pairs with finite momentum—that is, one that pairs particles at $\boldsymbol{Q} - \boldsymbol{k}$ and $\boldsymbol{Q} + \boldsymbol{k}$—is required to open a superconducting gap at Fermi surfaces which appear when the chemical potential μ is tuned to within a band. Figure 3 shows the condensation energy as a function of the boost momentum vector $\boldsymbol{Q}$. The stars indicate momenta corresponding to self-consistent mean-field states with the lowest energy, and it is at these momenta where a full pairing gap appears. An optimal boost moves the Fermi surface so that it becomes centered at $\boldsymbol{k} = \boldsymbol{G}/2$, where $\boldsymbol{G}$ is a reciprocal lattice vector (more information about the boost transformation can be found in Appendix B).
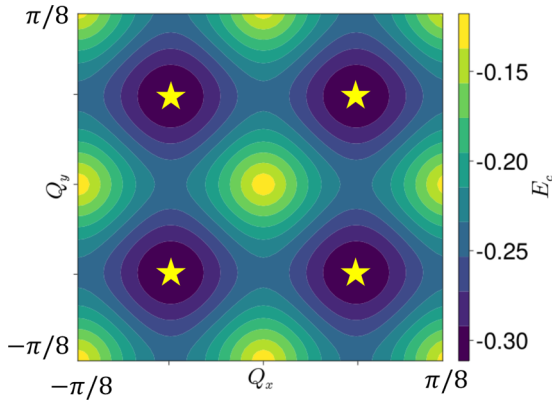

FIG. 3. Condensation energy as a function of the boost vector $\boldsymbol{Q}$ for $V_{sp} = 0.1$, $V_{SO} = 0.1$, $U = 3.2$, and $\mu = -3.48$ in the magnetic Brillouin zone. The stars indicate the minimum energy states. Note that states differing by a half reciprocal lattice vector have the same energy.

G. Chern number

We compute the Chern number, an integer-valued bulk topological invariant of the BdG Hamiltonian, to classify the system's topology. The non-Abelian formalism is used to avoid having to keep track of topological transitions of bands far below the Fermi level. We define the Berry connection in terms of its eigenvectors $|u^m(\boldsymbol{k})\rangle$:

$$A_\mu^{mn}(\boldsymbol{k}) = i\langle u^m(\boldsymbol{k})|\partial_\mu|u^n(\boldsymbol{k})\rangle, \qquad (19)$$

where $\partial_\mu \equiv \partial/\partial k_\mu$, $\mu = x, y$, and m, n are band indices. The Berry curvature is defined in terms of $A_\mu^{mn}(\boldsymbol{k})$,

$$F_{\mu\nu}^{mn}(\boldsymbol{k}) = \partial_\mu A_\nu^{mn} - \partial_\nu A_\mu^{mn} + i[A_\mu, A_\nu]^{mn}, \qquad (20)$$

and the Chern number is given by the integral over states with negative energy of the BdG Hamiltonian,

$$C = \frac{1}{2\pi} \int_{\text{MBZ}} d^2k \, \text{Tr}[F(\boldsymbol{k})]_{E(\boldsymbol{k})<0}. \qquad (21)$$

We numerically evaluate this integral using the method by Fukui *et al.* [88], which is highly efficient for gapped systems. The Berry curvature is determined on a grid in a discretized magnetic Brillouin zone (MBZ) by defining

$$M_\lambda^{mn}(\boldsymbol{k}_\alpha) = \langle u^m(\boldsymbol{k}_\alpha)|u^n(\boldsymbol{k}_\alpha + \boldsymbol{e}_\lambda)\rangle. \qquad (22)$$

The points on the grid are labeled by $\boldsymbol{k}_\alpha$ and the spacing vectors are $\boldsymbol{e}_\lambda$ where $\lambda = 1, 2$. In terms of the link variables defined as

$$U_\lambda(\boldsymbol{k}_\alpha) = \frac{\det M_\lambda(\boldsymbol{k}_\alpha)}{|\det M_\lambda(\boldsymbol{k}_\alpha)|}, \qquad (23)$$

the discrete Berry curvature at each point on the grid is given by

$$\tilde{F}(\boldsymbol{k}_\alpha) = \ln(U_1(\boldsymbol{k}_\alpha)U_2(\boldsymbol{k}_\alpha + \boldsymbol{e_1})U_1^{-1}(\boldsymbol{k}_\alpha + \boldsymbol{e_2})U_2^{-1}(\boldsymbol{k}_\alpha)). \qquad (24)$$

The Chern number is then given by

$$C = \frac{1}{2\pi i} \sum_\alpha \tilde{F}(\boldsymbol{k}_\alpha). \qquad (25)$$

When the Chern number is odd, the system is in the topological superconducting phase hosting non-Abelian Majorana quasiparticles. When the Chern number is even, the system does not host Majorana quasiparticles, and is in the same topological classification as a quantum Hall state. We find both possibilities in our results, but since both cases are, properly speaking, topological, we hereafter distinguish the former class of systems by referring to it as the non-Abelian topological phase.

III. RESULTS

We explored phase diagrams for a multitude of values of SOC and periodic potential strength for small Landau level filling factors (up to Landau level index $n = 8$), as shown in Fig. 4. The self-consistent mean-field equations were solved for each point on the phase diagrams, each of which consists of 6400 (80×80) points. For each point, guesses consisting of random complex numbers at each site within the MUC, as well as uniform real numbers, were used to start the iterative
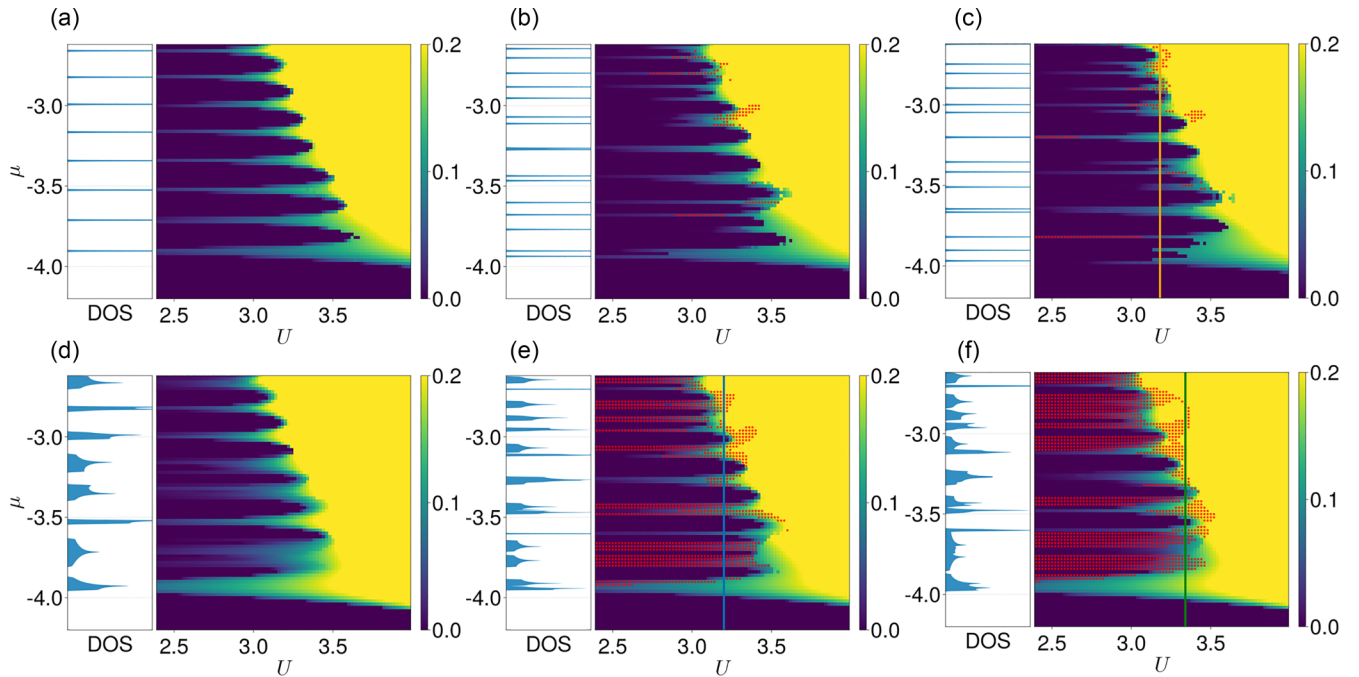
FIG. 4. The density of states of the system in the normal state on the left and the phase diagram on the right showing $\Delta_{\max}$ (color bar), the maximum value of the modulus of the self-consistent real-space pairing potential $|\Delta_j|$ in the ground state. The points where non-Abelian topological superconductivity is realized are denoted with small red stars. The parameters for each phase diagram are (a) $V_{SO} = 0$ and $V_{sp} = 0$, (b) $V_{SO} = 0.1 \approx \hbar\omega_c/2$ and $V_{sp} = 0$, (c) $V_{SO} = 0.15 \approx 3/2\hbar\omega_c$ and $V_{sp} = 0$, (d) $V_{SO} = 0$ and $V_{sp} = 0.2 \approx \hbar\omega_c$, (e) $V_{SO} = 0.1 \approx \hbar\omega_c/2$ and $V_{sp} = 0.1 \approx \hbar\omega_c/2$, and (f) $V_{SO} = 0.1 \approx \hbar\omega_c/2$ and $V_{sp} = 0.2 \approx \hbar\omega_c$. The self-consistency equations for all systems are solved, and the systems with a finite single-particle potential are boosted to an optimum value of $\boldsymbol{Q}$.

algorithm, and 16×16 (with flux $4\,h/e$) MUCs were used. The total energy was calculated for each solution [Eq. (16)] and the solution with the minimum energy was taken to be the ground-state solution. The color on the phase diagrams denotes $\Delta_{\max}$, the maximum value of the modulus of the self-consistent real-space pairing potential $|\Delta_j|$ in the ground state. The points marked with red stars are points where the system is in the non-Abelian phase; i.e., the Chern number is an odd integer. The corresponding density of states (DOS) in the normal state is shown to the left of each phase diagram. Let us now consider four different cases.

No SOC or superlattice potential. Figure 4(a) shows the phase diagram when both the SOC and single-particle potential are set to zero. The single-particle spectrum consists of spin-degenerate Landau levels, which have a band width on the order of 10^{-14} and their spacing (the cyclotron energy $\hbar\omega_c$) is approximately 0.2. The phase boundary separating nonsuperconducting and superconducting regions of the phase diagram displays substantial oscillatory behavior due to the Landau level structure. At lower interaction strength, superconductivity is present when the chemical potential is tuned to precisely the energy of a Landau level, but disappears when it is tuned to the gaps between different Landau levels. We hereafter refer to regions of enhanced superconductivity at Landau level energies as Landau level spikes. At larger interaction strength ($U \geqslant 3.5$), superconductivity is strongly augmented, and oscillations due to the Landau level structure disappear. We will refer to this region as the strong-pairing regime. The non-Abelian phase of topological superconductivity does not appear in the system without a periodic potential and SOC.

Instead, the Chern numbers for all of the points shown are even integers. This follows from the spin degeneracy of the energy levels (see Appendix E). In the weak-interaction portion of the phase diagram, when the energies are between Landau level spikes, the Chern number is 2ν where ν is the filling factor, consistent with the system being in a quantum Hall insulating phase. Within the Landau level spikes, the Chern number is an even integer, starting at 2ν when the interaction is weak, and decreases in even increments as the interaction is increased, until the strong-pairing regime where the Chern number is zero. It is interesting to note that superconductivity and nontrivial topology coincide on the Landau level spikes, although the topology is Abelian in nature.

SOC with no superlattice potential. Figures 4(b) and 4(c) show the phase diagrams of systems without the single-particle potential but with SOC strength $V_{SO} = 0.1$ and $V_{SO} = 0.15$, respectively. Due to nonzero SOC, the spin degeneracy of the Landau levels is lifted, and the energies are given approximately by

$$\epsilon_0 = \frac{1}{2}\hbar\omega_c - 4,$$

$$\epsilon_{m,\pm} = \hbar\omega_c\left(m \pm \sqrt{\frac{\pi}{4}\frac{V_{SO}^2}{\hbar^2\omega_c^2}m + \frac{1}{4}}\right) - 4 \quad (m > 0), \quad (26)$$

and accordingly there are Landau level spikes at these energies. Interestingly, we find small regions where the non-Abelian phase of topological superconductivity appears, most markedly at higher filling factors (at or around $\mu = -3$). For weaker interaction strength the Chern number at the
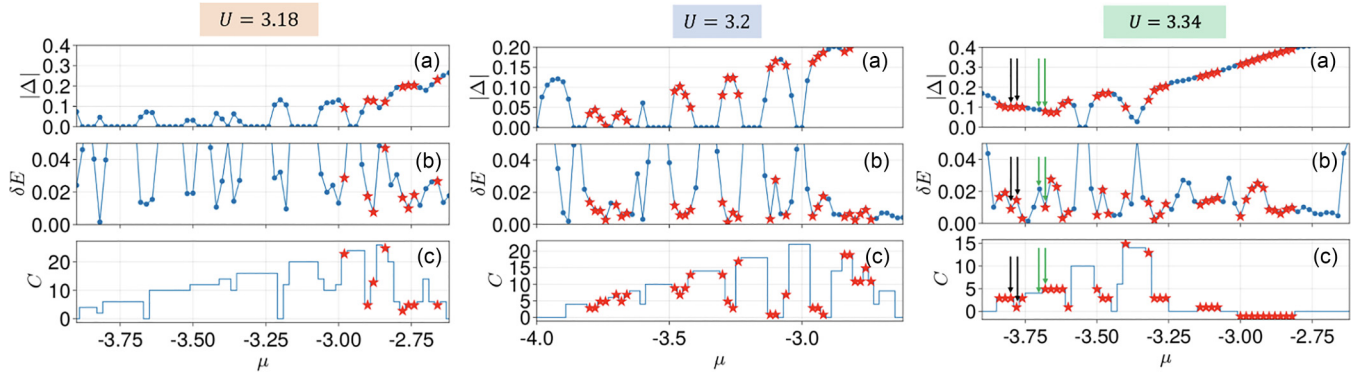
FIG. 5. (a) The maximum absolute value of the pairing potential; (b) the BdG spectral gap (δE); and (c) the Chern number (C) for systems with chemical potentials along the orange line in Fig. 4(c) at $U = 3.18$ (left panel), the blue line in Fig. 4(e) at $U = 3.2$ (middle panel), and the green line in Fig. 4(f) at $U = 3.34$ (right panel). The blue dots and red stars indicate systems we have studied. Blue dots correspond to systems with even Chern number and red stars correspond to systems with odd Chern number. The transitions indicated by the black and green arrows in the right panel are discussed in detail in the SM [76].

non-Abelian points is an odd integer close to twice the filling factor, and decreases as the interaction strength is increased, until the Chern number becomes zero in the strong-pairing regime. The vortex structure at these points will be discussed below. We remark that we do not find non-Abelian TSC arising from superconductivity in the lowest Landau level, which has been the subject of recent studies [51,52,54].

Plots of the maximum absolute value of the pairing potential, the BdG spectral gap (δE), and the Chern number (C), for chemical potentials along the orange line in Fig. 4(c), at fixed $U = 3.18$, are shown in the left panel of Fig. 5. Points where the system is in the non-Abelian phase are denoted with red stars. Oscillations in Fig. 5(a) (left panel) correspond to the Landau level spikes. The spectral gaps in Fig. 5(b) (left panel) come in two varieties: superconducting gaps and quantum Hall insulating gaps. The values of the quantum Hall insulating gaps, which occur when $\Delta = 0$, are given by $2\min(|\mu - \epsilon_{m\pm}|)$, and are much larger than superconducting gaps. When $\Delta \neq 0$, the gaps are superconducting gaps. Generally, the superconducting gaps are small, about an order of magnitude less than the cyclotron energy, in the regime where non-Abelian TSC appears. As seen in Fig. 5(c) (left panel), the Chern number exhibits discrete jumps as the chemical potential μ is tuned. These topological phase transitions come in two varieties: (1) transitions where the change in the Chern number is associated with a closing of the spectral gap, and (2) first-order transitions, where the Chern number changes without gap closing; these are associated with a change in the vortex lattice structure. This is discussed in detail with examples in the SM [76].

Superlattice potential with no SOC. Figure 4(d) shows the phase diagram for the system with periodic potential strength $V_{sp} = 0.2$ but without SOC. The optimum boost vector is used for each point on the phase diagram. Despite the Landau levels becoming significantly broadened, as can be seen in the DOS and in the corresponding smearing of the Landau level spikes, the non-Abelian phase does not appear, and the system transitions from an Abelian TSC or quantum Hall insulating phase at weak interaction to trivial superconductivity at stronger interaction. It comes as no surprise that we do not find the non-Abelian phase when there is a spin degeneracy.

This follows from Eqs. (19)–(21) and is established in detail in Appendix E.

Both superlattice potential and SOC. Finally, including both a single-particle potential and SOC leads to a considerable enhancement of non-Abelian TSC in the phase diagram. Figure 4(e) shows the phase diagram for $V_{sp} = 0.1$ and $V_{SO} = 0.1$, and Fig. 4(f) shows the phase diagram for $V_{sp} = 0.2$ and $V_{SO} = 0.1$. Non-Abelian TSC, which is marked using small red stars in the phase diagram, generally appears at the boundary between the quantum Hall insulator and superconducting phases, particularly along broadened Landau level spikes. Plots of the maximum absolute value of the pairing potential, the BdG spectral gap (δE), and the Chern number (C), for parameters along the blue line in Fig. 4(e) and the green line in Fig. 4(f), are shown in the middle panel of Fig. 5 and the right-hand panel of Fig. 5, respectively. Points where the system is in the non-Abelian phase are denoted with red stars. Oscillations can be seen in the middle panel of Fig. 5(a), and to a lesser degree in the right-hand panel of Fig. 5(a), which reflect the Landau level spikes. The spectral gaps are about an order of magnitude less than the cyclotron energy, at points where non-Abelian TSC appears. Again, we find topological phase transitions that come in the two varieties mentioned above (gap closing and first order).

A. Vortices and Majoranas

Due to the applied perpendicular magnetic field, the pairing potential experiences orbital frustration and Abrikosov vortices develop at the centers of which the pairing potential is zero. We find a plethora of configurations formed by the Abrikosov vortices, some of which are quite unexpected. As anticipated, Abrikosov vortices form a triangular lattice in the $n = 0$ and $n = 1$ Landau levels when the SOC and single-particle potential are absent. In addition we found square vortex lattice solutions with approximately 1–2 % higher energy than the triangular lattice solutions. With SOC, but without single-particle potential, a triangular lattice of vortices forms when the chemical potential is in the lowest five spin-split Landau levels—an example is shown in Fig. 6(a). In
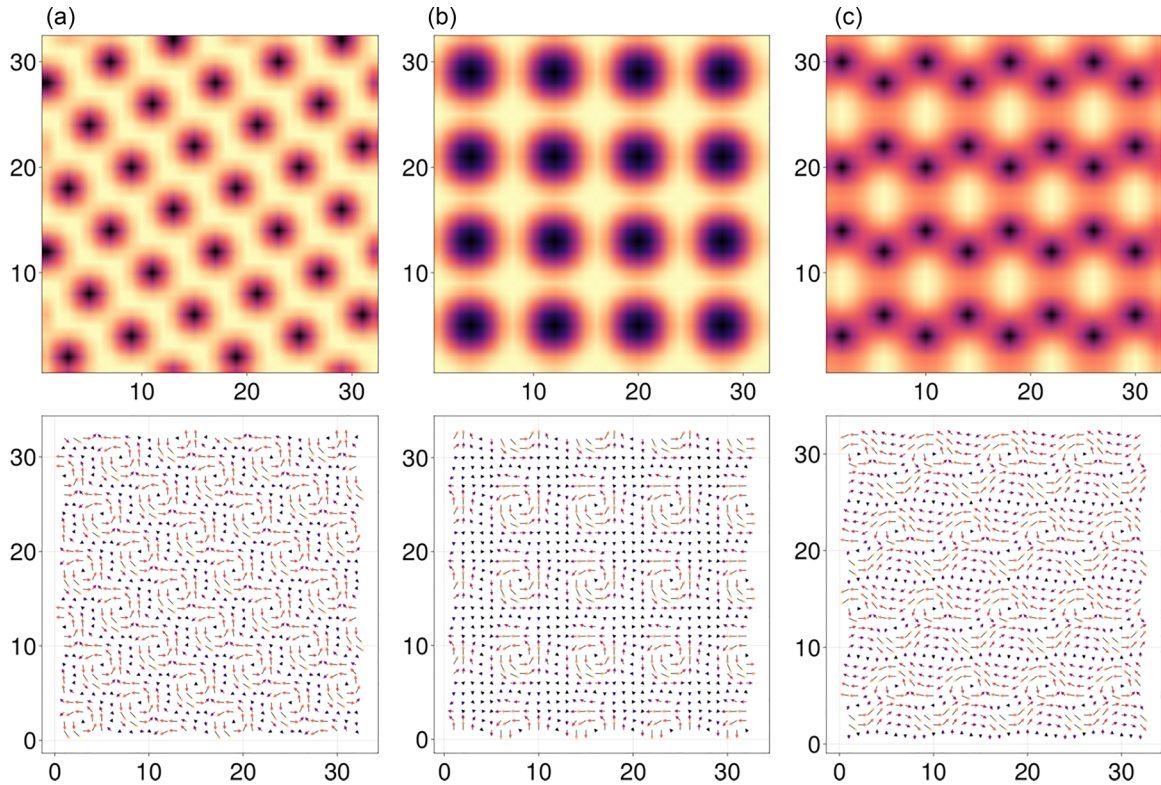
FIG. 6. Typical vortex lattice structures from the solutions to the self-consistent mean-field equations (upper panels) with their current textures (lower panels). (a) The vortex lattice at $V_{sp} = 0$, $V_{SO} = 0.1$, $U = 3.52$, and $\mu = -3.92$. In the lowest few Landau levels, the self-consistent solution is a triangular lattice of Abrikosov vortices carrying flux $h/2e$. (b) The vortex lattice at $V_{sp} = 0.2$, $V_{SO} = 0.1$, $U = 3.34$, and $\mu = -3.66$. The single-particle potential distorts the vortex lattice, drawing the vortices to areas of high potential energy. Typically in the topological region, the system forms a lattice of giant vortices. (c) The vortex lattice at $V_{sp} = 0$, $V_{SO} = 0.1$, $U = 3.24$, and $\mu = -3.08$. Other kinds of vortex order form at higher chemical potential (Landau level filling factor $\nu \approx 10$). For example, the vortices may form a (distorted) honeycomb lattice.

both cases, at higher chemical potential, the vortex structure is far more diverse. Of particular note is the vortex structure at topological points in Figs. 4(b) and 4(c), a typical example of which is shown in Fig. 6(c). Here the vortices form a honeycomb lattice, although not all the bonds are identical. Other interesting structures appear in the nontopological regions in the strong-pairing regime at chemical potential above the first few Landau levels. We show these in Fig. 7. Finally, when a single-particle potential is included, the vortices are distorted at all chemical potentials. In particular, vortices are drawn to locations where the single-particle potential is high. The vortices form dimer pairs, or combine to form giant vortices, consisting of two Abrikosov vortices. Topological points in Figs. 4(e) and 4(f) typically host the latter configuration [Fig. 6(b)].

As revealed by the finite gap when the system is in the non-Abelian topological phase, we do not find Majorana modes with zero energy in the bulk of the system. Instead the Majorana modes, which are thought to reside at vortex cores, hybridize with their neighbors and open a gap [9,10,12,13,52,89–98]. Nevertheless, because of the nontrivial Chern number and the bulk-boundary correspondence, we expect there to be chiral Majorana edge modes at the boundaries of samples in this phase.

IV. DISCUSSION

In this work, we investigated the emergence of TSC from topologically flat bands broadened by a superlattice potential. The robust SOC and the superlattice potential are essential components of our model. We comment on the relationship of our findings to potential materials platforms. A variety of systems have been discovered to exhibit superconductivity with strong SOC, including iron-based superconductors, interfaces of insulating oxides, and transition metal dichalcogenides [99,100]. More detailed, material-specific calculations would be required in the future to establish any specific candidate material, which is beyond the scope of this paper.

Our calculations have focused on a specific region of parameter space, which in our model contains a large number of parameters. It is important to identify candidate materials which might correspond to the parameter regime studied here. In the following discussion, we will express all energies in our calculations in units of the hopping amplitude t, which we have set to unity in our model. The cyclotron energy in our calculations is approximately 0.2. We have selected SOC strengths of 0.1 in the phase diagrams shown in Figs. 3(e) and 3(f). Our calculations are therefore directly applicable when the SOC strength is less than but close to the cyclotron energy. The cyclotron energy in real materials is determined
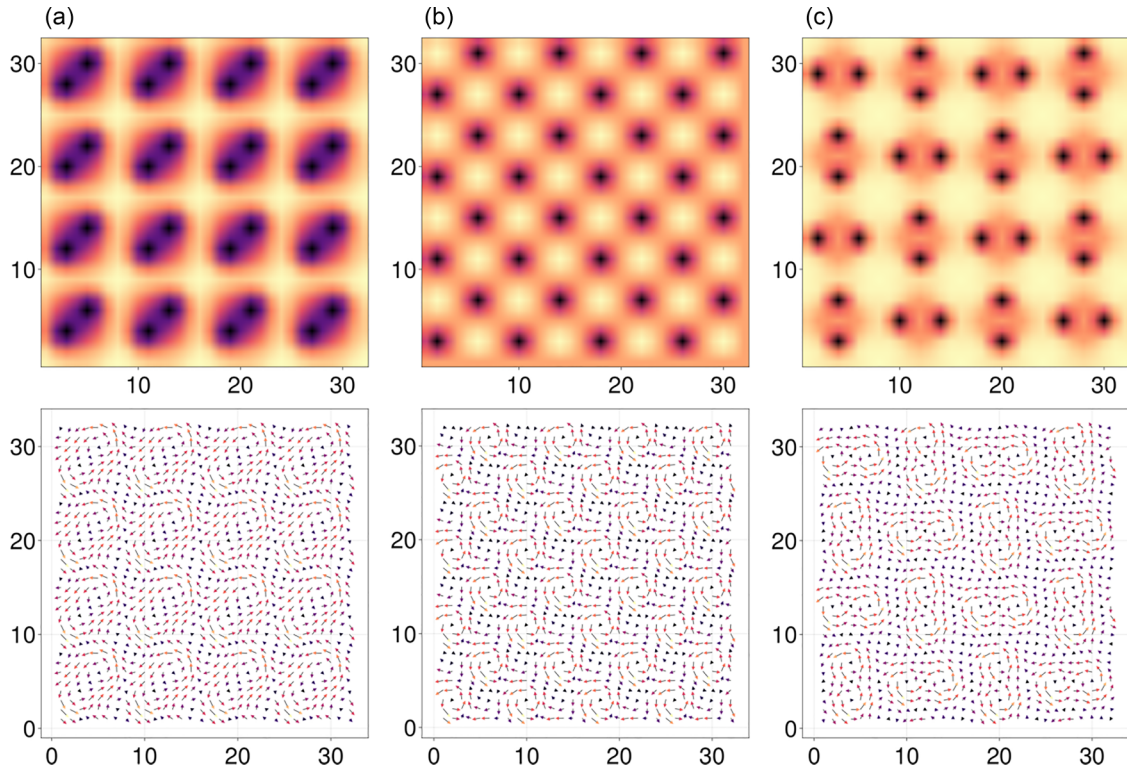
FIG. 7. Additional unexpected vortex lattice structures (above) from the solutions to the self-consistent mean-field equations with their current textures (below). (a) Dimer vortex configuration at $V_{\mathrm{sp}} = 0.2$, $V_{\mathrm{SO}} = 0.1$, $U = 3.48$, and $\mu = -3.66$. Dimer configurations of vortices can form due to the influence of the superlattice potential. We find that the appearance of dimerized vortices signals the exit from the non-Abelian topological phase. [(b) and (c)] Unexpected vortex configurations may appear even in the absence of a superlattice potential particularly at higher Landau level filling (or chemical potential). Shown here are (b) a stabilized square-lattice configuration at $V_{\mathrm{sp}} = 0$, $V_{\mathrm{SO}} = 0.1$, $U = 3.2$, and $\mu = -2.92$ and (c) a "double dimer" at $V_{\mathrm{sp}} = 0$, $V_{\mathrm{SO}} = 0.1$, $U = 3.54$, and $\mu = -3.22$.

by the effective mass m^*, as well as the strength of the applied magnetic field B through the formula

$$\hbar\omega_c = \hbar \frac{eB}{m^*}.$$

As an example, the cyclotron energy for bare electrons in a magnetic field of 20 T is estimated to be about 2 meV. Based on this information, we will now discuss some materials platforms individually. This is by no means intended to be an exhaustive list. A summary of relevant parameters for the following systems is provided in Table I.

Iron-based superconductors. The semimetallic iron pnictides and iron chalcogenides are a group of high-temperature superconductors that have generated significant enthusiasm in the condensed matter community since their discovery in 2008. These discoveries have ushered in a remarkable era of superconductivity known as the "iron age." The Rashba SOC in iron-based superconductors is found to be in the range 5–25 meV [101]. In addition, the pairing gap is found to be in this same range [101]. However, due to the strong interactions in these materials, the effective mass may be as high as 20 times the bare electron mass [102,115]. In order to model these materials, it may be preferable to take the SOC to be significantly greater than the cyclotron energy. It is anticipated that increasing the SOC will not diminish TSC, and we have performed additional calculations to support this claim. We show results for Rashba SOC strength of $V_{\mathrm{SO}} = 1.0$ (five times the cyclotron energy) in Fig. 8.

TABLE I. Estimates of key parameters in some select classes of spin-orbit-coupled superconductors. V_{SO} is the SOC strength, determined by the spin splitting at the Fermi level. Δ denotes the superconducting gap. m^* is the effective electron mass, expressed in terms of the bare electron mass m_e. $\hbar\omega_c$ is the cyclotron energy at a magnetic field of 20 T, computed using the material's effective electron mass. TMD, transition metal dichalcogenide.

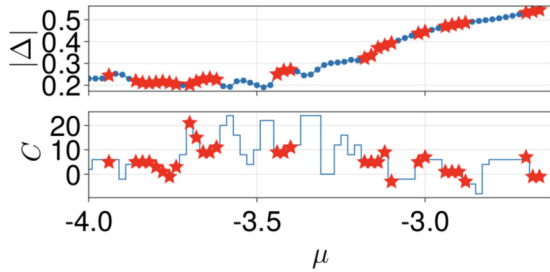| Material	V_{SO} (meV)	Δ (meV)	m^* (m_e)	$\hbar\omega_c$ (meV)
Iron-based thin films	5–25 [101]	5–25 [101,102]	10 [102]	0.2
LaAlO$_3$/SrTiO$_3$ interfaces	1–10 [103,104]	0.04 [105]	3 [103,106]	0.7
TMDs [107–114]	50–150 (Ising)	~1	~0.4	~6

FIG. 8. Topological superconductivity still appears (denoted with red stars) when the spin-orbit-coupling strength is high. In this figure, the spin-orbit-coupling strength is $V_{SO} = 1.0$, the superlattice potential strength is $V_{sp} = 0.2$, and the interaction strength $U = 3.98$. The Zeeman energy is zero.

Oxide interfaces. Superconductivity has been reported in the electron gas formed at the interfaces of $LaAlO_3$ and $SrTiO_3$ [116]. In addition, tunable Rashba SOC has been explored in this system with Rashba SOC strength in the range 1–10 meV [103,104]. The superconducting gap is found to be approximately 40 μeV [105] and the effective mass is $m^* = 3m_e$ where m_e is the electron mass [103,106]. Given these parameters, we are optimistic about the applicability of our results to this material platform.

Transition metal dichalcogenides. Superconductivity has been reported in layers of transition metal dichalcogenide (TMD) materials, resulting in 2D superconductivity. Examples of materials in this class include MoS_2, $MoSe_2$, WS_2, WSe_2, and $NbSe_2$. Layers of these materials break inversion symmetry within the plane, giving rise to Ising, SOC. Ising SOC tends to lock the electron spins perpendicular to the plane in a momentum-dependent way. In TMDs, this manifests as an effective Zeeman field with opposite signs at the K and K' points of the hexagonal Brillouin zone. Because of dominant Ising SOC our calculations are not readily applicable to these systems. However, Ising superconductivity still gives rise to a momentum-dependent spin splitting [117], so it may be worthwhile in the future to investigate the possibility of TSC using Ising SOC instead of Rashba SOC, as we did in our calculations. We point out that a crossover from Ising-dominant to Rashba-dominant SOC has also been recently observed in $NbSe_2/Bi_2Se_3$ heterostructures [118]. We hope that our study will stimulate inquiry along this direction.

In discussing the inclusion of a superlattice potential, the lattice period of the superlattice is an additional relevant parameter. Our calculations have focused on the case where the superlattice period is comparable to the magnetic length ℓ_B. The magnetic length is determined by the strength of the applied magnetic field B (in Tesla) through the formula

$$\ell_B = \sqrt{\frac{\hbar}{eB}} \approx \frac{25}{\sqrt{B}} \text{nm}.$$

For reference, $\ell_B \approx 6$ nm for a magnetic field $B = 20$ T. Below, we list systems where a superlattice potential may be achievable.

Gating periodic patterned dielectric substrates. The engineering of superlattices has been reported using patterned dielectrics, with strengths up to 50 meV and lattice periods as small as 35 nm [119–123]. In order to make direct connection with our results, let us suppose that the magnetic field $B \sim 20$ T, so that $\ell_B \approx 6$ nm. Thus, for our results to directly apply, it may be desirable to reduce the lattice period of the superlattice relative to what has been currently achieved. On physical grounds, however, we expect that TSC is readily achievable with large superlattice periods. This is because the superlattice potential brings about TSC through a distortion of the vortex lattice. This distortion is clearly possible with large superlattice periods. Therefore, we see gating periodic patterned dielectric substrates as a very promising route to inducing TSC using a superlattice potential.

Moiré patterns. A moiré pattern can be formed by stacking layers of materials with a relative twist, in which case the lattice vectors of the two layers are relatively rotated by an angle θ, or by stacking materials with slightly mismatched lattice periodicities. The moiré pattern leads to a periodic potential with a periodicity determined by θ with a strength on the order of hundreds of meV [124] in bilayer MoS_2. Exciting recent progress has been reported in the fabrication of van der Waals superconducting heterostructures wherein moiré patterns have been achieved [125]. Since materials from this class typically host Ising spin-orbit coupling instead of Rashba spin-orbit coupling, further calculations would be required to make a firm connection between our proposal and these materials. Finally, we comment on the connection of the parameters of our "effective" model to an experimental system. Our phase diagram shows TSC at rather large $U \sim 3$, an order of magnitude larger than the cyclotron energy. However, the gap Δ for these values of U is roughly of the same order of magnitude as the cyclotron energy. In experiments, it is the pairing gap Δ that is typically measured rather than the coupling strength U between electrons. Therefore, in order to relate our findings to experimental data, the parameter U in our model should be fixed by matching the gap Δ to its experimental value. We have listed some values of Δ for systems that we discussed in the previous paragraphs in Table I.

Previously, the helical phase of superconductors was discussed in the context of noncentrosymmetric superconductors using Ginzburg-Landau theory [84–86,126]. Certain terms, known as Lifshitz invariants, can be eliminated from the free energy by performing a helical (or in our language, boost) transformation when inversion symmetry is broken. This is a similar procedure to the one we employ, albeit in a microscopic theory. However, even in the absence of Rashba SOC when inversion symmetry is preserved, helical transformations are necessary in our model because of the presence of a magnetic field and superlattice potential.

This work has demonstrated the dramatic influence on the vortex lattice structure by a superlattice potential, in the case of $\ell_B/a_M \approx 1$, where ℓ_B is the magnetic length and a_M is the superlattice vector. Understanding the vortex lattice structure for other values of ℓ_B/a_M, particularly irrational values, and the corresponding topological properties in this model, will be left for future work.

Finally, we would like to discuss some issues related to realizing intrinsic quantum Hall superconductivity. It has been over 50 years since quantum Hall superconductivity was first explored [127]; however, due to the requirement of low

densities or very high magnetic fields, it has not been achieved in experiments. In addition, theoretical studies on intrinsic quantum Hall superconductivity, including this one, have relied on mean-field theories which do not allow for all possible instabilities. In a real material, the interaction will be a mixture of attractive and repulsive, and this may lead to competition between other correlated phases including, but not limited to, FQHE, stripe phases, charge density waves, and spin density waves. The question of whether other strongly correlated phases may arise, particularly in the case of flat LLs, is an interesting question beyond mean-field theory, which we leave for the future.

ACKNOWLEDGMENTS

APPENDIX A: DERIVATION OF THE EXPRESSION FOR THE NET CURRENT

In the main text, we pointed out that the condition that the energy be minimized with respect to Q implies that the net current vanishes, since the net current is $J_{\text{net}} = \frac{\delta \mathcal{E}_{\text{MF}}}{\delta Q}$. In this Appendix, we derive this expression for the net current. The current density across a link starting at position r_i along the μ direction ($\mu = x,\,y$) is

$$J_\mu(r_i) = -\frac{\partial \mathcal{H}_{\text{MF}}}{\partial A_\mu(r_i)}, \tag{A1}$$

where $A_\mu(r_i)$ is the hopping phase across the same link and $\mathcal{H}_{\text{MF}}$ is the mean-field Hamiltonian. The net current in the μ direction is the sum over all of the sites of $J_\mu(r_i)$:

$$(J_{\text{net}})_\mu = -\sum_i \frac{\partial \mathcal{H}_{\text{MF}}}{\partial A_\mu(r_i)}. \tag{A2}$$

As we have pointed out in the main text, shifting Q is equivalent to shifting all of the hopping phases by a position-independent amount $A(r_j) \rightarrow A(r_j) - Q$. Under a small shift δQ, the change in $\mathcal{H}_{\text{MF}}$, to first order in δQ, is given by

$$\mathcal{H}_{\text{MF}}(\{A_\mu(r_i) - \delta Q_\mu\})$$
$$= \mathcal{H}_{\text{MF}}(\{A_\mu(r_i)\}) - \sum_{\mu=x,y} \delta Q_\mu \sum_i \frac{\partial \mathcal{H}_{\text{MF}}}{\partial A_\mu(r_i)}$$
$$= \mathcal{H}_{\text{MF}}(\{A_\mu(r_i)\}) + \delta Q \cdot J_{\text{net}}. \tag{A3}$$

Therefore, we have,

$$(J_{\text{net}})_\mu = \frac{\delta \mathcal{H}_{\text{MF}}}{\delta Q_\mu}. \tag{A4}$$

Taking the ground-state expectation value (and using the Feynman-Hellmann theorem), we find $J_{\text{net}} = \frac{\delta \mathcal{E}_{\text{MF}}}{\delta Q}$.

APPENDIX B: BOOSTS

Nonrelativistic physics is invariant under Galilean boosts, whereas relativistic physics is invariant under Lorentz boosts. In classical mechanics, the transformation rule for a Galilean boost by velocity v is

$$\bar{x} = x + vt,$$
$$\bar{t} = t. \tag{B1}$$

This increases the velocity of every particle in the system by v.

Continuing to the quantum mechanical case, suppose we have N identical fermions with mass m and momenta $k_1 \neq k_2 \neq \cdots \neq k_N$. We will neglect spin for the moment since Galilean boosts do not affect the spins of the particles. The action of a Galilean boost is given by an operator $U_B(v)$ which acts on a first-quantized momentum eigenstate as follows:

$$U_B(v)|k_1, \ldots, k_N\rangle = |k_1 + mv, \ldots, k_N + mv\rangle. \tag{B2}$$

To deduce the operator form of $U_B(v)$, we determine its action on position space eigenkets. In fact,

$$U_B(v)|x_1, \ldots, x_N\rangle$$
$$= \frac{1}{L^N} \sum_{\{k\}} \exp\left(-i\sum_i k_i \cdot x_i\right) U_B(v)|k_1, \ldots, k_N\rangle$$
$$= \frac{1}{L^N} \sum_{\{k\}} \exp\left(-i\sum_i k_i \cdot x_i\right) |k_1 + mv, \ldots, k_N + mv\rangle$$
$$= \frac{1}{L^N} \sum_{\{k\}} \exp\left(-i\sum_i (k_i - mv) \cdot x_i\right) |k_1, \ldots, k_N\rangle$$
$$= \exp\left(imv \cdot \sum_i x_i\right) |x_1, \ldots, x_N\rangle, \tag{B3}$$

so we see that the position kets are eigenstates of the boost operator. This also allows us to deduce that the operator form of $U_B(v)$ is

$$U_B(v) = \exp(imv \cdot X) = \exp(iMv \cdot R_{\text{c.m.}}), \tag{B4}$$

where $X = \sum_i x_i$ is the sum of the positions of all the particles, $M = \sum_i m_i = Nm$ is the total mass of the system, and $R_{\text{c.m.}}$ is the center-of-mass coordinate of the system. We see that $U_B(v)$ is unitary. Using the form $U_B(v) = \exp(imv \cdot X)$, we can write $U_B(v)$ in second-quantized representation as

$$U_B(v) = \exp\left(imv \cdot \int d^2r\, r c_r^\dagger c_r\right). \tag{B5}$$

For notational consistency with the main text, we will set $mv = Q$ and define $U_B(v) \equiv U_B(Q)$. Now consider the action of $U_B(Q)$ on the field operators. We have (we may use the Baker-Campbell-Hausdorff formula to show this)

$$\bar{c}_r := U_B^\dagger(Q) c_r U_B(Q) = c_r e^{iQ \cdot r}, \tag{B6}$$

where barred operators are operators for the "boosted frame." As an example, let us apply this boost to a system of free

spinless fermions described by the Hamiltonian

$$\mathcal{H} = \sum_{k} (\epsilon(k) - \mu) c_{k}^{\dagger} c_{k}, \tag{B7}$$

where $c_{k} = \frac{1}{L} \sum_{r} e^{-ik \cdot r} c_{r}$. Note that by Eq. (B6), we have

$$U_{B}^{\dagger}(Q) c_{k} U_{B}(Q) = \bar{c}_{k} = c_{k-Q}. \tag{B8}$$

Suppose we view the system in Eq. (B7) in a frame boosted by Q; then the Hamiltonian $\bar{\mathcal{H}}$ in this frame is

$$\begin{aligned}
\bar{\mathcal{H}} = U_{B}^{\dagger}(Q) \mathcal{H} U_{B}(Q) &= \sum_{k} (\epsilon(k) - \mu) \bar{c}_{k}^{\dagger} \bar{c}_{k} \\
&= \sum_{k} (\epsilon(k) - \mu) c_{k-Q}^{\dagger} c_{k-Q} \\
&= \sum_{k} (\epsilon(k+Q) - \mu) c_{k}^{\dagger} c_{k}. \tag{B9}
\end{aligned}$$

It will be useful to see how the ground states in the laboratory and boosted frames are related. In the laboratory frame, the ground state is

$$|\Phi_{0}\rangle = \left(\prod_{\substack{k \text{ s.t.} \\ \epsilon(k) < \mu}} c_{k}^{\dagger} \right) |0\rangle, \tag{B10}$$

whereas in the boosted frame

$$\begin{aligned}
|\bar{\Phi}_{0}\rangle &= \left(\prod_{\substack{k \text{ s.t.} \\ \epsilon(k) < \mu}} \bar{c}_{k}^{\dagger} \right) |0\rangle = \left(\prod_{\substack{k \text{ s.t.} \\ \epsilon(k) < \mu}} c_{k-Q}^{\dagger} \right) |0\rangle \\
&= \left(\prod_{\substack{k \text{ s.t.} \\ \epsilon(k+Q) < \mu}} c_{k}^{\dagger} \right) |0\rangle. \tag{B11}
\end{aligned}$$

These are related as

$$|\Phi_{0}\rangle = U_{B}(Q) |\bar{\Phi}_{0}\rangle. \tag{B12}$$

This relation holds generally and can be used to find the ground state in the laboratory frame once the ground state in the boosted frame is known.

As a simple example to elucidate the procedure in the main text, we may take a lattice system, in zero magnetic field, described by the Hamiltonian

$$\mathcal{H} = \sum_{k,\sigma} (\epsilon(k) - \mu) c_{k\sigma}^{\dagger} c_{k\sigma} - U \sum_{j} c_{j,\uparrow}^{\dagger} c_{j,\downarrow}^{\dagger} c_{j,\downarrow} c_{j,\uparrow}, \tag{B13}$$

where $\epsilon(k) = -2(\cos k_{x} + \cos k_{y})$. We perform a mean-field decoupling with a helical ansatz, as discussed in the main article, to determine the self-consistent superconducting ground state. The condensation energies are shown in Fig. 9, which is used to determined the ground state, and the accompanying Bogoliubov–de Gennes spectra for several boost vectors Q are
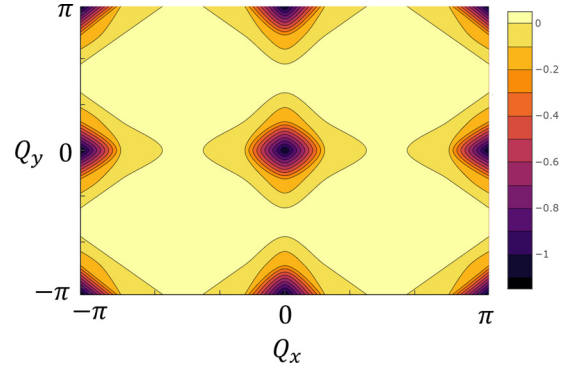

FIG. 9. The total energy, measured relative to the normal state (i.e., the condensation energy), as a function of the boost vector Q. The hopping amplitude in the square-lattice model has been set to unity. The minima occur when the Fermi surface is situated such that $k_{+} + k_{-} = G$, where $k_{\pm}$ are momenta on opposite sides of the Fermi surface and G is a reciprocal lattice vector. See Fig. 10.

shown in Fig. 10, where it can be seen how it changes for different choices of Q.

APPENDIX C: ALGORITHM

Algorithm 1 is an algorithm to solve the mean-field problem self-consistently. Its inputs are the dimensions of the MUC, which contains $\Phi = n\Phi_{0}$ flux where $n \in \mathbb{Z}$ ($\Phi_{0} = h/e$ is the flux quantum), the interaction strength U, the chemical potential μ, the spin-orbit-coupling strength V_{SO}, the superlattice potential strength V_{sp}, and the initial guess for the s-wave pairing potential $\Delta_{j}^{(0)}$. Its outputs are the Gor'kov Green's function $\mathcal{G}(k)$ and the mean-field ground-state energy $\mathcal{E}_{\text{MF}}$ of the system.

Algorithm 1. Iterative algorithm for solving the mean-field equations.

Require: $M, N, n, U, \mu, V_{\text{SO}}, V_{\text{sp}}, \Delta_{j}^{(0)}$

Ensure: $\Delta_{j}, \mathcal{G}(k) \forall k \in \text{MBZ}, \mathcal{E}_{\text{MF}}$
    Build the diagonal blocks of $H_{\text{BdG}}(k)$ using $h(k)$,
    $\Sigma(k) \forall k \in \text{HBZ}$;
    $\delta\Delta = \infty$;
    $l = 0$
    While $\delta\Delta > \tau$ **do** ▷ The tolerance for differences in Δ is $\tau = 10^{-5}$.
        Update/build $\Delta_{\downarrow\uparrow}$ using $\Delta_{j}^{(l)}$;
        for $k \in \text{HBZ}$**do**
            Update off-diagonal blocks of $H_{\text{BdG}}(k)$ using $\Delta_{\downarrow\uparrow}$;
            Compute $\mathcal{G}(k)$ by diagonalization of $H_{\text{BdG}}(k)$, using (17)
            and particle-hole symmetry for $\mathcal{G}(-k)$;
            Do a running sum to compute $\Delta_{j}^{(l+1)}$;
        end for
        Compute pairing potential difference
        $\delta\Delta = \max_{j} (|\Delta_{j}^{(l+1)} - \Delta_{j}^{(l)}|)$;
        $l \leftarrow l + 1$;
    end While
    Compute $\mathcal{E}_{\text{MF}}$

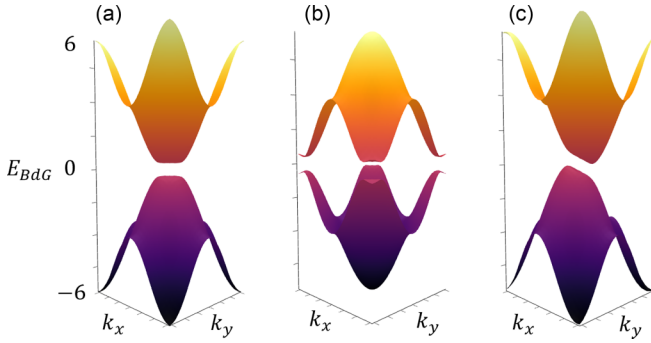FIG. 10. The Bogoliubov–de Gennes spectrum for boost vectors (a) at the minimum energy point $Q = 0$, where it can be seen that a robust pairing gap opens; (b) at the minimum energy point $Q = (\pi, \pi)$, where it can be seen that a robust pairing gap also opens; and (c) slightly away from $Q = 0$. In general, away from the minimum energy Q, one generally finds small indirect gaps, or indirect gap closings in the spectrum.
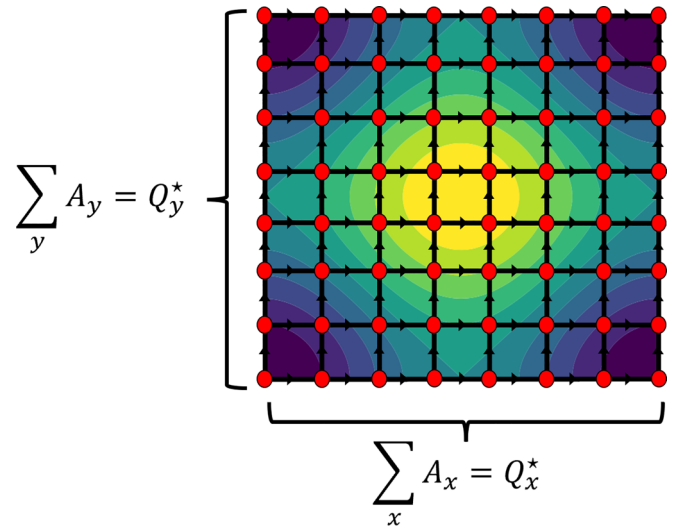

FIG. 11. The unit cell of the superlattice potential used in the main text. The color plot underneath the lattice shows the contours of the potential with the maximum denoted in bright yellow and the minimum in deep blue. For a given choice of gauge A, an optimum boost vector (one that leads to the lowest mean-field energy) is given by the sum of the hopping phases along edges connecting the minima of the superlattice potential.

APPENDIX D: HOW TO DETERMINE AN OPTIMUM BOOST VECTOR ANALYTICALLY

For a particular gauge, the sum of the hopping phases along edges linking the minima of the superlattice potential determines an optimum boost vector (one that results in the lowest mean-field energy). See Fig. 11. Such a boost leads to zero accumulated phase for particles with $k = 0$ traversing the unit cell of the potential in both the x and y directions, thereby respecting the C_4 symmetry of the superlattice potential and resulting in the minimum energy.

APPENDIX E: THE REASON THERE IS NO TSC WHEN $V_{\mathrm{SO}} = 0$

We do not find topological superconductivity without spin-orbit coupling. This follows from the spin degeneracy in the spectrum of our BdG Hamiltonian in the absence of spin-orbit coupling. Without spin-orbit coupling, the mean-field Hamiltonian reads

$$\mathcal{H}_{\mathrm{MF}} = -\sum_{j,\delta,\sigma}(e^{iA_\delta(\boldsymbol{r}_j)}c_{j+\delta,\sigma}^\dagger c_{j,\sigma} + e^{-iA_\delta(\boldsymbol{r}_j)}c_{j,\sigma}^\dagger c_{j+\delta,\sigma}) - \sum_{j,\sigma}(\mu - V(\boldsymbol{r}_j))c_{j,\sigma}^\dagger c_{j\sigma} - \sum_j \left(\Delta_j c_{j,\uparrow}^\dagger c_{j,\downarrow}^\dagger + \Delta_j^* c_{j,\downarrow} c_{j,\uparrow} - \frac{|\Delta_j|^2}{U}\right). \tag{E1}$$

Consider the spin-flip operator $\hat{F}$ defined as $\hat{F} c_{j,\sigma} \hat{F}^\dagger = c_{j,-\sigma}$. Clearly the hopping and chemical potential terms are invariant under the operation of F. The action of F on the pairing term is

$$\hat{F}\mathcal{H}_\Delta \hat{F}^\dagger = -\sum_j \left(\Delta_j c_{j,\downarrow}^\dagger c_{j,\uparrow}^\dagger + \Delta_j^* c_{j,\uparrow} c_{j,\downarrow} - \frac{|\Delta_j|^2}{U}\right) = -\sum_j \left(-\Delta_j c_{j,\uparrow}^\dagger c_{j,\downarrow}^\dagger - \Delta_j^* c_{j,\downarrow} c_{j,\uparrow} - \frac{|\Delta_j|^2}{U}\right). \tag{E2}$$

So $\mathcal{H}_\Delta$ is, strictly speaking, not invariant under $\hat{F}$. It is, however, invariant up to a global gauge transformation which renders $\Delta_j \to -\Delta_j$. Thus, the mean-field Hamiltonian has a symmetry $\hat{S} = e^{-i\hat{N}\pi/2}\hat{F}$ where $\hat{N} = \sum_{j,\sigma} c_{j,\sigma}^\dagger c_{j\sigma}$. Under this symmetry, the eigenvectors of the BdG Hamiltonian generally transform as

$$\begin{pmatrix} u_\uparrow(\boldsymbol{k}) \\ u_\downarrow(\boldsymbol{k}) \\ v_\uparrow(\boldsymbol{k}) \\ v_\downarrow(\boldsymbol{k}) \end{pmatrix} \to i \begin{pmatrix} u_\downarrow(\boldsymbol{k}) \\ u_\uparrow(\boldsymbol{k}) \\ -v_\downarrow(\boldsymbol{k}) \\ -v_\uparrow(\boldsymbol{k}) \end{pmatrix}. \tag{E3}$$

A spin-up state has the form $(u(\boldsymbol{k}) \quad 0 \quad 0 \quad v(\boldsymbol{k}))^{\mathrm{T}}$ and so the corresponding spin-down state is $i(0 \quad u(\boldsymbol{k}) \quad -v(\boldsymbol{k}) \quad 0)^{\mathrm{T}}$.

Constructing the Berry connection matrix out of these two bands, we see that

$$A_\mu^{\downarrow\downarrow}(\boldsymbol{k}) = i[u^*(\boldsymbol{k})\partial_\mu u(\boldsymbol{k}) + v^*(\boldsymbol{k})\partial_\mu v(\boldsymbol{k})] \tag{E4}$$

and we find the same result for $A_\mu^{\uparrow\uparrow}(\boldsymbol{k})$. The Berry curvatures for these bands are thus the same: $F_{\mu\nu}^{\uparrow\uparrow}(\boldsymbol{k}) = F_{\mu\nu}^{\downarrow\downarrow}(\boldsymbol{k})$. The Chern number for these bands is given by

$$C = \frac{1}{2\pi}\int_{\mathrm{MBZ}} d^2k[F_{xy}^{\uparrow\uparrow}(\boldsymbol{k}) + F_{xy}^{\downarrow\downarrow}(\boldsymbol{k})]$$

$$= 2\frac{1}{2\pi}\int_{\mathrm{MBZ}} d^2k[F_{xy}^{\uparrow\uparrow}(\boldsymbol{k})] \in 2\mathbb{Z}. \tag{E5}$$
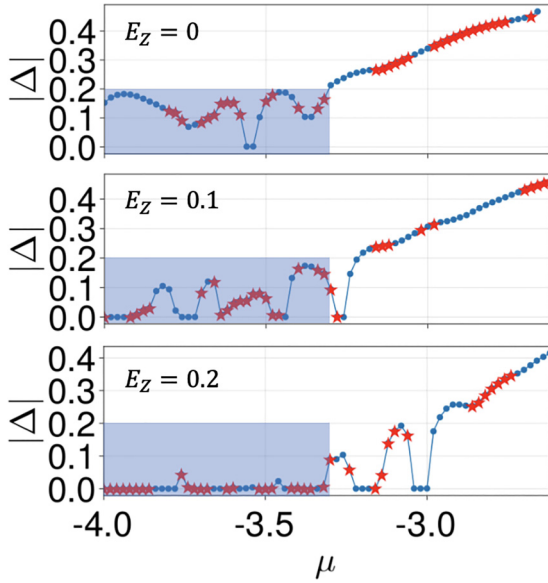
FIG. 12. The pairing potential is reduced based on the Pauli limit. When the value of E_Z reaches 0.2, all the points with pairing potential less than or equal to approximately 0.2 in the absence of Zeeman field ($\mu \approx -4$ to $\mu \approx -3.3$, highlighted with a blue rectangle) are significantly reduced. However, we still find topological superconductivity (denoted with red stars). Here we have set the attractive interaction $U = 3.38$, the superlattice potential strength $V_{sp} = 0.2$, and the spin-orbit coupling strength $V_{SO} = 0.1$.

Therefore, the sum of the Chern numbers from all the filled bands is an even integer, thus excluding the non-Abelian topological phase.

APPENDIX F: ROLE OF ZEEMAN FIELD

We find that, upon including the Zeeman effect into the calculation, superconductivity is suppressed due to the Pauli limit,

$$E_Z^P \approx |\Delta|, \tag{F1}$$

where E_Z^P is the Pauli-limited Zeeman energy and Δ is the pairing potential. However, TSC survives. This is shown in Fig. 12 and described in detail in the caption.

APPENDIX G: EMERGENCE OF p-WAVE SUPERCONDUCTIVITY

In this section, we comment on the emergence of the p-wave component of superconductivity in our model, which can arise from s-wave superconductivity and Rashba spin-orbit coupling due to singlet-triplet mixing [128,129], as inversion symmetry is broken by Rashba spin-orbit coupling
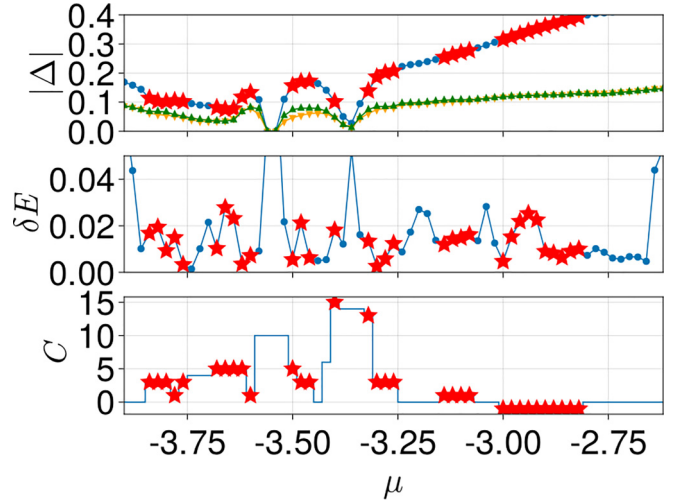

FIG. 13. Top: The blue dots and red stars are the maximum absolute value of the pairing potential. Blue dots correspond to systems with even Chern number and red stars correspond to systems with odd Chern number. The green triangles are $10U \max(|\Psi_{j\downarrow+}|)$ and the orange triangles are $10U \max(|\Psi_{j\downarrow+}|)$. Middle: The BdG spectral gap (δE). Bottom: The Chern number (C). The parameters are $U = 3.34$, $V_{sp} = 0.2$, and $V_{SO} = 0.1$ (the same as in Fig. 6 of the main article).

[99]. We explicitly show this by calculating p-wave components of the order parameter.

Let us define

$$\Psi_{j\sigma\delta} = \langle c_{j,\sigma} c_{j+\delta,\sigma} \rangle. \tag{G1}$$

The expectation values can be determined from the Gor'kov Green's function (see the SM [76]). It is convenient to transform these variables to the $p_x + ip_y$ component $\Psi_{j\sigma+}$ and $p_x - ip_y$ component $\Psi_{j\sigma-}$:

$$\Psi_{j\sigma+} = \tfrac{1}{2}[\Psi_{j\sigma\hat{x}} - i\Psi_{j\sigma\hat{y}}],$$
$$\Psi_{j\sigma-} = \tfrac{1}{2}[\Psi_{j\sigma\hat{x}} + i\Psi_{j\sigma\hat{y}}]. \tag{G2}$$

Out of the components $\Psi_{j\uparrow+}$, $\Psi_{j\downarrow+}$, $\Psi_{j\uparrow-}$, and $\Psi_{j\downarrow-}$, we find that $\Psi_{j\uparrow-}$ and $\Psi_{j\downarrow+}$ are dominantly the largest. In Fig. 13, we show these components, together with the s-wave component, for parameters $U = 3.34$, $V_{sp} = 0.2$, and $V_{SO} = 0.1$ (the same as in Fig. 6 of the main article). The green curve in the upper panel is $10U \max(|\Psi_{j\downarrow+}|)$ and the orange curve in the upper panel is $10U \max(|\Psi_{j\downarrow+}|)$. The curve with blue dots and red stars is $\max(|\Delta_j|) = U \max(|\langle c_{j,\downarrow} c_{j,\uparrow} \rangle|)$. It is thus clear that the s-wave component is much larger than the p-wave component by roughly a factor of 60. We also see that the emergence of a p-wave component accompanies the appearance of *superconductivity*, not just *topological* superconductivity. This is to be expected because superconductors with broken parity and time-reversal symmetries typically exhibit singlet-triplet mixing.

[1] M. Stone and S.-B. Chung, Phys. Rev. B **73**, 014505 (2006).

[2] M. Oshikawa, Y. B. Kim, K. Shtengel, C. Nayak, and S. Tewari, Ann. Phys. **322**, 1477 (2007).

[3] C. Nayak, S. H. Simon, A. Stern, M. Freedman, and S. Das Sarma, Rev. Mod. Phys. **80**, 1083 (2008).

[4] J. D. Sau, R. M. Lutchyn, S. Tewari, and S. Das Sarma, Phys. Rev. Lett. **104**, 040502 (2010).

[5] T. D. Stanescu, J. D. Sau, R. M. Lutchyn, and S. Das Sarma, Phys. Rev. B **81**, 241310(R) (2010).

[6] J. Alicea, Rep. Prog. Phys. **75**, 076501 (2012).

[7] H.-H. Hung, P. Ghaemi, T. L. Hughes, and M. J. Gilbert, Phys. Rev. B **87**, 035401 (2013).

[8] C. Beenakker, Annu. Rev. Condens. Matter Phys. **4**, 113 (2013).

[9] J. Zhou, Y.-J. Wu, R.-W. Li, J. He, and S.-P. Kou, Europhys. Lett. **102**, 47005 (2013).

[10] R. R. Biswas, Phys. Rev. Lett. **111**, 136401 (2013).

[11] S. D. Sarma, M. Freedman, and C. Nayak, npj Quantum Inf. **1**, 15001 (2015).

[12] T. Liu and M. Franz, Phys. Rev. B **92**, 134519 (2015).

[13] J. M. Murray and O. Vafek, Phys. Rev. B **92**, 134520 (2015).

[14] E. D. B. Smith, K. Tanaka, and Y. Nagai, Phys. Rev. B **94**, 064515 (2016).

[15] D. Chowdhury, A. Georges, O. Parcollet, and S. Sachdev, Rev. Mod. Phys. **94**, 035004 (2022).

[16] B. A. Bernevig, *Topological Insulators and Topological Superconductors* (Princeton University Press, Princeton, NJ, 2013).

[17] S. Das Sarma, C. Nayak, and S. Tewari, Phys. Rev. B **73**, 220502(R) (2006).

[18] L. Fu and C. L. Kane, Phys. Rev. Lett. **100**, 096407 (2008).

[19] R. M. Lutchyn, J. D. Sau, and S. Das Sarma, Phys. Rev. Lett. **105**, 077001 (2010).

[20] X.-L. Qi, T. L. Hughes, and S.-C. Zhang, Phys. Rev. B **82**, 184516 (2010).

[21] J. D. Sau, S. Tewari, R. Lutchyn, T. D. Stanescu, and S. Das Sarma, Phys. Rev. B **82**, 214509 (2010).

[22] J. Alicea, Phys. Rev. B **81**, 125318 (2010).

[23] X.-L. Qi and S.-C. Zhang, Rev. Mod. Phys. **83**, 1057 (2011).

[24] A. M. Black-Schaffer, Phys. Rev. B **83**, 060504(R) (2011).

[25] V. Mourik, K. Zuo, S. M. Frolov, S. Plissard, E. P. Bakkers, and L. P. Kouwenhoven, Science **336**, 1003 (2012).

[26] S. Nakosai, Y. Tanaka, and N. Nagaosa, Phys. Rev. Lett. **108**, 147003 (2012).

[27] T. D. Stanescu and S. Tewari, J. Phys.: Condens. Matter **25**, 233201 (2013).

[28] S. L. Goertzen, K. Tanaka, and Y. Nagai, Phys. Rev. B **95**, 064509 (2017).

[29] R. M. Lutchyn, E. P. Bakkers, L. P. Kouwenhoven, P. Krogstrup, C. M. Marcus, and Y. Oreg, Nat. Rev. Mater. **3**, 52 (2018).

[30] Y. Oreg, G. Refael, and F. von Oppen, Phys. Rev. Lett. **105**, 177002 (2010).

[31] S. Nadj-Perge, I. K. Drozdov, J. Li, H. Chen, S. Jeon, J. Seo, A. H. MacDonald, B. A. Bernevig, and A. Yazdani, Science **346**, 602 (2014).

[32] C.-X. Liu, J. D. Sau, T. D. Stanescu, and S. Das Sarma, Phys. Rev. B **96**, 075161 (2017).

[33] S. Frolov, M. Manfra, and J. Sau, Nat. Phys. **16**, 718 (2020).

[34] J. Klinovaja, P. Stano, A. Yazdani, and D. Loss, Phys. Rev. Lett. **111**, 186805 (2013).

[35] J. Li, H. Chen, I. K. Drozdov, A. Yazdani, B. A. Bernevig, and A. H. MacDonald, Phys. Rev. B **90**, 235433 (2014).

[36] T.-P. Choy, J. M. Edge, A. R. Akhmerov, and C. W. J. Beenakker, Phys. Rev. B **84**, 195442 (2011).

[37] S. Nadj-Perge, I. K. Drozdov, B. A. Bernevig, and A. Yazdani, Phys. Rev. B **88**, 020407(R) (2013).

[38] F. Pientka, L. I. Glazman, and F. von Oppen, Phys. Rev. B **88**, 155420 (2013).

[39] A. Fornieri, A. M. Whiticar, F. Setiawan, E. Portolés, A. C. Drachmann, A. Keselman, S. Gronin, C. Thomas, T. Wang, R. Kallaher *et al.*, Nature (London) **569**, 89 (2019).

[40] F. Pientka, A. Keselman, E. Berg, A. Yacoby, A. Stern, and B. I. Halperin, Phys. Rev. X **7**, 021032 (2017).

[41] P. Marra, J. Appl. Phys. **132**, 231101 (2022).

[42] H. Lu, S. Das Sarma, and K. Park, Phys. Rev. B **82**, 201303(R) (2010).

[43] D. J. Clarke, J. Alicea, and K. Shtengel, Nat. Commun. **4**, 1348 (2013).

[44] R. S. K. Mong, D. J. Clarke, J. Alicea, N. H. Lindner, P. Fendley, C. Nayak, Y. Oreg, A. Stern, E. Berg, K. Shtengel, and M. P. A. Fisher, Phys. Rev. X **4**, 011036 (2014).

[45] J. Alicea and A. Stern, Phys. Scr. T **164**, 014006 (2015).

[46] J. Alicea and P. Fendley, Annu. Rev. Condens. Matter Phys. **7**, 119 (2016).

[47] F. Amet, C. T. Ke, I. V. Borzenets, J. Wang, K. Watanabe, T. Taniguchi, R. S. Deacon, M. Yamamoto, Y. Bomze, S. Tarucha, and G. Finkelstein, Science **352**, 966 (2016).

[48] J. Liang, G. Simion, and Y. Lyanda-Geller, Phys. Rev. B **100**, 075155 (2019).

[49] Ö. Gül, Y. Ronen, S. Y. Lee, H. Shapourian, J. Zauberman, Y. H. Lee, K. Watanabe, T. Taniguchi, A. Vishwanath, A. Yacoby *et al.*, Phys. Rev. X **12**, 021057 (2022).

[50] D. Shaffer, J. Wang, and L. H. Santos, Phys. Rev. B **104**, 184501 (2021).

[51] B. Zocher and B. Rosenow, Phys. Rev. B **93**, 214504 (2016).

[52] R. V. Mishmash, A. Yazdani, and M. P. Zaletel, Phys. Rev. B **99**, 115427 (2019).

[53] G. S. Jeon, J. K. Jain, and C.-X. Liu, Phys. Rev. B **99**, 094509 (2019).

[54] G. Chaudhary and A. H. MacDonald, Phys. Rev. B **101**, 024516 (2020).

[55] V. Pathak, S. Plugge, and M. Franz, Ann. Phys. **435**, 168431 (2021).

[56] A. K. Rajagopal and R. Vasudevan, Phys. Rev. B **44**, 2807 (1991).

[57] Z. Tešanović, M. Rasolt, and L. Xing, Phys. Rev. Lett. **63**, 2425 (1989).

[58] Z. Tešanović, M. Rasolt, and L. Xing, Phys. Rev. B **43**, 288 (1991).

[59] M. R. Norman, Phys. Rev. Lett. **66**, 842 (1991).

[60] H. Akera, A. H. MacDonald, S. M. Girvin, and M. R. Norman, Phys. Rev. Lett. **67**, 2375 (1991).

[61] A. K. Rajagopal and J. C. Ryan, Phys. Rev. B **44**, 10280 (1991).

[62] M. Rasolt and Z. Tesanovic, Rev. Mod. Phys. **64**, 709 (1992).

[63] A. H. MacDonald, H. Akera, and M. R. Norman, Phys. Rev. B **45**, 10147 (1992).

[64] M. Norman, H. Akera, and A. MacDonald, Phys. C (Amsterdam, Neth.) **196**, 43 (1992).

[65] A. K. Rajagopal, Phys. Rev. B **46**, 1224 (1992).

[66] A. MacDonald, H. Akera, and M. Norman, Aust. J. Phys. **46**, 333 (1993).

[67] J. Ryan and A. Rajagopal, J. Phys. Chem. Solids **54**, 1281 (1993).

[68] J. C. Ryan and A. K. Rajagopal, Phys. Rev. B **47**, 8843 (1993).

[69] M. R. Norman, A. H. MacDonald, and H. Akera, Phys. Rev. B **51**, 5927 (1995).

[70] M. M. Maśka, Phys. Rev. B **66**, 054533 (2002).

[71] P. Scherpelz, D. Wulin, B. Šopík, K. Levin, and A. K. Rajagopal, Phys. Rev. B **87**, 024516 (2013).

[72] S. Ran, C. Eckberg, Q. Ding, Y. Furukawa, T. Metz, S. Saha, I. Liu, M. Zic, H. Kim, J. Paglione *et al.*, Science **365**, 684 (2019).

[73] T. Kim, C.-C. Chien, and S.-Z. Lin, Phys. Rev. B **99**, 054509 (2019).

[74] G. Chaudhary, A. H. MacDonald, and M. R. Norman, Phys. Rev. Res. **3**, 033260 (2021).

[75] P. Fulde and R. A. Ferrell, Phys. Rev. **135**, A550 (1964).

[76] See Supplemental Material at http://link.aps.org/supplemental/10.1103/PhysRevB.109.134518 for details on particle-hole symmetry, construction of the mean-field groundstate, construction of the Gor'kov Green's function and writing correlation functions, derivation of an expression for the current operator, derivation of the spin-orbit coupling Hamiltonian, and a close examination of cases where the spectral gap closes and re-opens across Chern number-changing transitions. This includes a reference to M. Ezawa, Y. Tanaka, and N. Nagosa, Sci. Rep. **3**, 1 (2013).

[77] P. G. Harper, Proc. Phys. Soc. A **68**, 874 (1955).

[78] M. Y. Azbel, Sov. Phys. JETP **19**, 634 (1964).

[79] J. Zak, Phys. Rev. **134**, A1602 (1964).

[80] E. Brown, Phys. Rev. **133**, A1038 (1964).

[81] J. Zak, Phys. Rev. **134**, A1607 (1964).

[82] D. R. Hofstadter, Phys. Rev. B **14**, 2239 (1976).

[83] K. Yang and D. F. Agterberg, Phys. Rev. Lett. **84**, 4970 (2000).

[84] R. P. Kaur, D. F. Agterberg, and M. Sigrist, Phys. Rev. Lett. **94**, 137002 (2005).

[85] D. F. Agterberg and R. P. Kaur, Phys. Rev. B **75**, 064511 (2007).

[86] D. F. Agterberg, *Non-Centrosymmetric Superconductors* (Springer, Berlin, 2012), pp. 155–170.

[87] S. Mironov and A. Buzdin, Phys. Rev. Lett. **118**, 077001 (2017).

[88] T. Fukui, Y. Hatsugai, and H. Suzuki, J. Phys. Soc. Jpn. **74**, 1674 (2005).

[89] E. Grosfeld and A. Stern, Phys. Rev. B **73**, 201303(R) (2006).

[90] M. Cheng, R. M. Lutchyn, V. Galitski, and S. Das Sarma, Phys. Rev. Lett. **103**, 107001 (2009).

[91] M. Cheng, R. M. Lutchyn, V. Galitski, and S. Das Sarma, Phys. Rev. B **82**, 094504 (2010).

[92] A. W. Ludwig, D. Poilblanc, S. Trebst, and M. Troyer, New J. Phys. **13**, 045014 (2011).

[93] Y. E. Kraus and A. Stern, New J. Phys. **13**, 105006 (2011).

[94] V. Lahtinen, A. W. W. Ludwig, J. K. Pachos, and S. Trebst, Phys. Rev. B **86**, 075115 (2012).

[95] C. R. Laumann, A. W. W. Ludwig, D. A. Huse, and S. Trebst, Phys. Rev. B **85**, 161301(R) (2012).

[96] M. A. Silaev, Phys. Rev. B **88**, 064514 (2013).

[97] D. Ariad, E. Grosfeld, and B. Seradjeh, Phys. Rev. B **92**, 035136 (2015).

[98] C. Li and M. Franz, Phys. Rev. B **98**, 115123 (2018).

[99] E. Bauer and M. Sigrist, *Non-centrosymmetric Superconductors: Introduction and Overview* (Springer, Berlin, 2012), Vol. 847.

[100] M. Smidman, M. Salamon, H. Yuan, and D. Agterberg, Rep. Prog. Phys. **80**, 036501 (2017).

[101] S. Borisenko, D. Evtushinsky, Z.-H. Liu, I. Morozov, R. Kappenberger, S. Wurmehl, B. Büchner, A. Yaresko, T. Kim, M. Hoesch *et al.*, Nat. Phys. **12**, 311 (2016).

[102] S. Haindl, *Iron-Based Superconducting Thin Films* (Springer, Berlin, 2021).

[103] A. D. Caviglia, M. Gabay, S. Gariglio, N. Reyren, C. Cancellieri, and J.-M. Triscone, Phys. Rev. Lett. **104**, 126803 (2010).

[104] K. V. Shanavas and S. Satpathy, Phys. Rev. Lett. **112**, 086802 (2014).

[105] G. Singh, G. Venditti, G. Saiz, G. Herranz, F. Sánchez, A. Jouan, C. Feuillet-Palma, J. Lesueur, M. Grilli, S. Caprara, and N. Bergeal, Phys. Rev. B **105**, 064512 (2022).

[106] L. Mattheiss, Phys. Rev. B **6**, 4740 (1972).

[107] X. Xi, L. Zhao, Z. Wang, H. Berger, L. Forró, J. Shan, and K. F. Mak, Nat. Nanotechnol. **10**, 765 (2015).

[108] X. Xi, Z. Wang, W. Zhao, J.-H. Park, K. T. Law, H. Berger, L. Forró, J. Shan, and K. F. Mak, Nat. Phys. **12**, 139 (2016).

[109] M. M. Ugeda, A. J. Bradley, Y. Zhang, S. Onishi, Y. Chen, W. Ruan, C. Ojeda-Aristizabal, H. Ryu, M. T. Edmonds, H.-Z. Tsai *et al.*, Nat. Phys. **12**, 92 (2016).

[110] H. Wang, X. Huang, J. Lin, J. Cui, Y. Chen, C. Zhu, F. Liu, Q. Zeng, J. Zhou, P. Yu *et al.*, Nat. Commun. **8**, 1 (2017).

[111] S. C. de la Barrera, M. R. Sinko, D. P. Gopalan, N. Sivadas, K. L. Seyler, K. Watanabe, T. Taniguchi, A. W. Tsen, X. Xu, D. Xiao *et al.*, Nat. Commun. **9**, 1427 (2018).

[112] D. Xiao, G.-B. Liu, W. Feng, X. Xu, and W. Yao, Phys. Rev. Lett. **108**, 196802 (2012).

[113] Z. Y. Zhu, Y. C. Cheng, and U. Schwingenschlögl, Phys. Rev. B **84**, 153402 (2011).

[114] K. Kośmider, J. W. González, and J. Fernández-Rossier, Phys. Rev. B **88**, 245436 (2013).

[115] J. Baglo, J. Chen, K. Murphy, R. Leenen, A. McCollam, M. L. Sutherland, and F. M. Grosche, Phys. Rev. Lett. **129**, 046402 (2022).

[116] N. Reyren, S. Thiel, A. Caviglia, L. F. Kourkoutis, G. Hammerl, C. Richter, C. W. Schneider, T. Kopp, A.-S. Ruetschi, D. Jaccard *et al.*, Science **317**, 1196 (2007).

[117] Y.-T. Hsu, A. Vaezi, M. H. Fischer, and E.-A. Kim, Nat. Commun. **8**, 14985 (2017).

[118] H. Yi, L.-H. Hu, Y. Wang, R. Xiao, J. Cai, D. R. Hickey, C. Dong, Y.-F. Zhao, L.-J. Zhou, R. Zhang *et al.*, Nat. Mater. **21**, 1366 (2022).

[119] C. Forsythe, X. Zhou, K. Watanabe, T. Taniguchi, A. Pasupathy, P. Moon, M. Koshino, P. Kim, and C. R. Dean, Nat. Nanotechnol. **13**, 566 (2018).

[120] M. Yankowitz, J. Jung, E. Laksono, N. Leconte, B. L. Chittari, K. Watanabe, T. Taniguchi, S. Adam, D. Graf, and C. R. Dean, Nature (London) **557**, 404 (2018).

[121] L.-k. Shi, J. Ma, and J. C. Song, 2D Mater. **7**, 015028 (2020).

[122] Y. Xu, C. Horn, J. Zhu, Y. Tang, L. Ma, L. Li, S. Liu, K. Watanabe, T. Taniguchi, J. C. Hone *et al.*, Nat. Mater. **20**, 645 (2021).

[123] Y. Li, S. Dietrich, C. Forsythe, T. Taniguchi, K. Watanabe, P. Moon, and C. R. Dean, Nat. Nanotechnol. **16**, 525 (2021).

[124] N. Tilak, G. Li, T. Taniguchi, K. Watanabe, and E. Y. Andrei, Nano Lett. **23**, 73 (2023).

[125] Z. Zhou, F. Hou, X. Huang, G. Wang, Z. Fu, W. Liu, G. Yuan, X. Xi, J. Xu, J. Lin, and L. Gao, Nature (London) **621**, 499 (2023).

[126] D. Agterberg, Physica C (Amsterdam, Neth.) **387**, 13 (2003).

[127] A. Rajagopal and R. Vasudevan, Phys. Lett. **20**, 585 (1966).

[128] L. P. Gor'kov and E. I. Rashba, Phys. Rev. Lett. **87**, 037004 (2001).

[129] P. A. Frigeri, D. F. Agterberg, A. Koga, and M. Sigrist, Phys. Rev. Lett. **92**, 097001 (2004).